

## ESD ACCESSION LIST

TRI Call No. 76154Copy No. 1 of 2 cys.

TRI FILE COPY

## ESD RECORD COPY

RETURN TO  
SCIENTIFIC & TECHNICAL INFORMATION DIVISION  
(TRI), Building 1210

1

Solid State Research

1972

Prepared under Electronic Systems Division Contract F19628-70-C-0230 by

**Lincoln Laboratory**

MASSACHUSETTS INSTITUTE OF TECHNOLOGY

Lexington, Massachusetts



AD740874



Approved for public release; distribution unlimited.

1

# Solid State Research

1972

Issued 12 April 1972

Prepared under Electronic Systems Division Contract F19628-70-C-0230 by

## Lincoln Laboratory

MASSACHUSETTS INSTITUTE OF TECHNOLOGY

Lexington, Massachusetts



Approved for public release; distribution unlimited.

The work reported in this document was performed at Lincoln Laboratory, a center for research operated by Massachusetts Institute of Technology, with the support of the Department of the Air Force under Contract F19628-70-C-0230.

This report may be reproduced to satisfy needs of U.S. Government agencies.

Non-Lincoln Recipients

**PLEASE DO NOT RETURN**

Permission is given to destroy this document  
when it is no longer needed.

#### ABSTRACT

This report covers in detail the solid state research work of the Solid State Division at Lincoln Laboratory for the period 1 November 1971 through 31 January 1972. The topics covered are Solid State Device Research, Quantum Electronics, Materials Research, Physics of Solids, and Microelectronics. The Microsound work is sponsored by ABMDA and is reported under that program.

Accepted for the Air Force  
Joseph R. Waterman, Lt. Col., USAF  
Chief, Lincoln Laboratory Project Office

# CONTENTS

Abstract	iii
Introduction	vii
Reports on Solid State Research	xii
Organization	xvii
I. SOLID STATE DEVICE RESEARCH	1
A. Detectivity Measurements on Guarded InSb n-p Junctions Fabricated Using Proton Bombardment	1
B. InSb p-n Junction Photodiodes Fabricated by Zn <sup>+</sup> Ion Implantation	1
C. K-Band BaAs IMPATT Diodes	2
D. Magnetic-Field-Tuned PbSSe Lasers for High-Resolution Spectroscopy	5
E. Optically Pumped Pb <sub>1-x</sub> Ge <sub>x</sub> Te and Pb <sub>1-x</sub> Ge <sub>x</sub> S Lasers	7
II. QUANTUM ELECTRONICS	9
A. Diode-Pumped In <sub>x</sub> Ga <sub>1-x</sub> As and InP Lasers	9
B. Broadband Laser Emission from Optically Pumped PbS <sub>x</sub> Se <sub>1-x</sub>	13
C. High-Resolution Spectroscopy of Atmospheric Water Vapor	15
D. Determination of Total Band Intensity and Transition Moment for the $\nu_1$ -Band of SO <sub>2</sub>	16
III. MATERIALS RESEARCH	19
A. Energy Bands in TX <sub>2</sub> Compounds with Pyrite, Marcasite, and Arsenopyrite Structures	19
B. Effect of Carrier Gas Velocity on Supersaturation Required for Vapor Phase Crystal Growth	24
C. Impurity Profiles of Evaporated Gold Films Determined by Auger Electron Spectroscopy	27
D. Pb-Rich Solidus of PbS <sub>0.63</sub> Se <sub>0.37</sub>	29
IV. PHYSICS OF SOLIDS	33
A. Phosphor Upconversion	33
1. Rare-Earth Phosphors for Near-Infrared-to-Visible Upconversion	33
2. Infrared Stimulation of Visible Luminescence in ZnS Phosphors	34
B. Laser Spectroscopy	35
1. Resolved Q-Branch Absorption in Nitric Oxide: Nuclear Hyperfine Splitting	35
2. Measurement of the Gain Lineshape of a CO Gas Laser Using a Tunable Semiconductor Laser	39
3. Tunable PbTe Laser Spectroscopy at 6.5 $\mu$ m	40
4. Molecular Systems Optically Pumped with TEA Lasers	42

## Contents

C. Infrared Properties of Solids	43
1. High-Resolution Far-Infrared Investigation of Hydrogenic Impurities in Ultrapure Germanium	43
2. Far-Infrared-Reflectivity Study of Paratellurite	43
3. Microscopic Theory of the Spontaneous Spin-Flip Raman Lineshape in InSb	46
V. MICROELECTRONICS	49
A. Mask-Making Laboratory	49
B. Semiconductor Devices Area	50
C. Applications of Electron-Beam Evaporation Technology	51
D. Bonding and Assembly	52



# INTRODUCTION

## I. SOLID STATE DEVICE RESEARCH

Infrared detectivity measurements have been made on InSb n-p junction photodiodes that have annular guard-ring field plates to control the surface potential at the n-p junction. At 77°K, 20-mil-diameter circular devices whose junctions were formed by proton bombardment have zero-bias resistances as high as 20 megohms at the optimum field-plate voltage, and in reduced background these diodes have detectivities as large as  $2.75 \times 10^{12} \text{ cm}\sqrt{\text{Hz}}/\text{W}$  at a wavelength of 5.3  $\mu\text{m}$ .

InSb p-n junction photodiodes have been fabricated by the implantation of 400-kV zinc ions into n-type crystals. For 20-mil-diameter diodes at 77°K zero-bias, resistances of 1 to 3 megohms have been observed. In reduced background the peak detectivity of these diodes is about  $10^{12} \text{ cm}\sqrt{\text{Hz}}/\text{W}$  at 5.3  $\mu\text{m}$ . The quantum efficiency is about 60 percent at 5.3  $\mu\text{m}$  for diodes without an antireflection coating, and remains high to wavelengths as short as 1  $\mu\text{m}$ .

A CW oscillator output power of 380 mW at 28 GHz with an efficiency of 6.8 percent has been achieved with an epitaxial GaAs Schottky barrier IMPATT diode having an active device diameter of 2 mils. A similar p-n junction device delivered 275 mW of CW power at 32 GHz with an efficiency of 7.8 percent. This device also produced 13 dB of small signal gain at comparable frequencies when operated as an amplifier.

Magnetic field tuning over a range of about 2 percent of the laser energy has been observed for  $\text{PbS}_{1-x}\text{Sc}_x$  diode lasers at 10°K. For a  $\text{PbS}_{0.82}\text{Se}_{0.18}$  diode, the laser gain spectrum was found to shift at a rate of about  $0.44 \text{ cm}^{-1}/\text{kG}$ , whereas the fine tuning rate of an individual mode of a  $\text{PbS}_{0.61}\text{Sc}_{0.39}$  diode laser was about 1 MHz/kG.

Laser emission has been observed in vapor-grown  $\text{Pb}_{1-x}\text{Ge}_x\text{Te}$  and  $\text{Pb}_{1-x}\text{Ge}_x\text{S}$  crystals optically pumped using a GaAs diode laser source. For two different compositions of  $\text{Pb}_{1-x}\text{Ge}_x\text{Te}$ , the wavelengths at 10°K were 5.4 and 5.27  $\mu\text{m}$ , respectively, and for a  $\text{Pb}_{1-x}\text{Ge}_x\text{S}$  crystal the wavelength was 3.43  $\mu\text{m}$  at 10°K and 3.33  $\mu\text{m}$  at 40°K. These results suggest that the two materials are potentially useful for fabricating diode lasers throughout the 3.4- to 6.6- $\mu\text{m}$  wavelength range.

## II. QUANTUM ELECTRONICS

Laser emission spectra were observed from  $\text{In}_x\text{Ga}_{1-x}\text{As}$  and InP crystals pumped at low temperature by pulsed GaAs diode lasers. From the axial mode spacing, an effective index of refraction is found which is much larger than that observed for diode lasers of similar materials. This increase occurs because the emission frequencies of the optically pumped lasers are much closer to the band edge than are the emission frequencies of the diodes. Mode broadening occurs at high temperatures, and may be attributable to chirping caused by increased heating arising from the increased pump intensity necessary for high-temperature



operation. At high temperatures, two separate sets of modes in InP have been observed separated by  $\sim 6 \text{ \AA}$ . This corresponds to the transverse mode spacing predicted by an  $\sim 20\text{-}\mu\text{m}$ -wide guiding region.

A Q-switched YAG laser has been used to optically pump  $\text{PbS}_x\text{Se}_{1-x}$  crystals at low temperature. A single alloy composition crystal operated as a laser over a range of up to 10 percent of the center frequency. This provides a fractional tuning range comparable to a dye laser. By using several alloy compositions, laser action has been observed from 3.9 to 8.6  $\mu\text{m}$ .

Three water-vapor absorption lines were studied at atmospheric pressure using a tunable  $\text{PbS}_x\text{Se}_{1-x}$  diode laser. The lines were identified and their widths, strengths, and relative positions were measured. Comparing present results with earlier work, we find that these high J lines are a factor of 2 to 4 narrower than previously estimated, the strengths agree within experimental error, and the relative line positions differ by several hundredths of a wave number.

Work continues on determining parameters of the  $\nu_1$ -band of  $\text{SO}_2$  using tunable laser spectroscopy. The intensities of several isolated lines were measured. From these data, the total band strength was found to be  $358 \pm 20 \times 10^{-20} \text{ cm}^{-1} \text{ mol}^{-1} \text{ cm}^2$ , and the effective vibrational transition moment was determined to be  $0.086 \pm 0.003 \text{ D}$ .

### III. MATERIALS RESEARCH

The principal features of the energy bands for transition metal  $\text{TX}_2$  compounds crystallizing in the pyrite, marcasite, and arsenopyrite structures have been derived on the basis of symmetry arguments and the conceptual phase diagrams previously developed. The structure-determining interactions are argued to be cation-anion interactions, not cation-cation interactions. Except in the  $\text{MnX}_2$  chalcogenides and  $\text{CrSb}_2$ , the 3d-electrons appear to be itinerant rather than localized, and the crystallographic determinant is not the conventional Jahn-Teller mechanism.

The growth of ZnTe crystals from the vapor phase in an open tube system has been studied in order to determine the effect of carrier gas velocity on the degree of supersaturation required for nucleation and growth. At the lowest velocities, the difference between the temperature at which the carrier gas was saturated and the temperature required for nucleation was  $20^\circ$  to  $30^\circ\text{C}$ . With increasing velocity, the temperature difference decreased to a minimum of essentially zero at Reynolds numbers of 1000 to 2000 and then increased significantly.

Auger electron spectroscopy has been used to determine impurity profiles of  $200\text{-}\text{\AA}$ -thick gold films deposited by evaporation on Pyrex which has first been coated with a very thin layer of nichrome (Ni, Cr, Fe) or Kanthal (Fe, Cr, Al). After the gold-nichrome-Pyrex composite has been annealed at  $600^\circ\text{C}$  in air for 16 hours (the procedure used to obtain adhering films for transparent furnaces), the Ni and most of the Fe are found at the outer surface of the gold, while most of the Cr remains at the gold-Pyrex interface.

## IV. PHYSICS OF SOLIDS

The phosphor upconversion studies have continued. In gagarinite ( $\text{NaY}_{0.81}\text{Yb}_{0.18}\text{Er}_{0.01}\text{F}_4$ ), the excitation and emission spectra have been investigated. Also, measurements of the phosphor efficiency have been made; primary efforts have concentrated on increasing the near-infrared input intensity in an attempt to establish the upper bounds of achievable efficiency. In the ZnS phosphor program, infrared stimulation measurements on a nominally undoped ZnS indicate a behavior which is qualitatively identical to that observed in doped ZnS:Cu,Al. Preliminary solutions to the rate equations for one set of values of the various parameters indicate results qualitatively in accord with experiment.

In the high-resolution laser spectroscopy program, studies of the fundamental vibration-rotation bands of nitric oxide have now been extended to Q branches. Several lines near the head of both the  $Q_{1/2}$  and  $Q_{3/2}$  branches have been fully resolved for the first time; both  $\Lambda$ -type doubling and nuclear hyperfine structure are observed for the first few  $Q_{1/2}$  absorption lines.

The frequency gain(loss) profile of several vibrational-rotational lines of a CO gas laser amplifier was measured using a tunable PbSe laser operating near  $5.3\text{ }\mu\text{m}$ . With a linewidth of  $<1\text{ MHz}$ , the current-tuned semiconductor laser completely resolves the lineshape of each individual line.

High-resolution spectra have also been obtained in methane, nitrogen dioxide, and water vapor by means of a current-tuned PbTe diode laser emitting near  $6.5\text{ }\mu\text{m}$ .

The recently developed technique of obtaining submillimeter radiation from molecular gases by optically pumping with  $\text{CO}_2$  lasers on a quasi-CW basis has been extended to the high-power regime by use of a  $\text{CO}_2$  TEA laser ( $\sim 0.7\text{ MW}$ ). In addition to increasing the submillimeter power output, a large number of previously unreported lines were found in  $\text{CH}_3\text{OH}$  and  $\text{CH}_3\text{F}$ .

In other high-resolution infrared studies, the photoconductivity spectral response of n-type ultrapure ( $\sim 2 \times 10^{10}\text{ donors/cm}^3$ ) germanium was investigated by Fourier spectroscopy in the range  $60$  to  $120\text{ cm}^{-1}$  and at liquid helium temperatures. The spectral response appears to be due to four hydrogen-like series of transitions, two of which have been tentatively identified from earlier low-resolution studies as arising from antimony and phosphorous donors. Previously unobserved structure, due to transitions to the higher excited  $p^\pm$  and  $f^\pm$  levels of hydrogen-like shallow donors, has been found and identified.

The room-temperature far-infrared reflectivity of paratellurite,  $\text{TeO}_2$ , has been investigated from  $50$  to  $400\text{ cm}^{-1}$  using a Fourier spectrometer. Due to the presence of optical activity, transparency from  $0.33$  to  $6.5\text{ }\mu\text{m}$ , strongly birefringent refractive indices, an extremely slow  $\langle 110 \rangle$  shear wave, and a lack of center of inversion,  $\text{TeO}_2$  appears promising for piezoelectric, acousto-optic, and nonlinear optical applications.

The spontaneous spin-flip linewidth is an important parameter which affects the gain, threshold, and fine tuning of the spin-flip Raman laser. In an effort to understand theoretically the lineshape in n-type InSb, the effects of ionized impurity scattering at low temperatures have

been derived by means of a Bethe-Salpeter transport equation. The results are similar to those obtained previously by using a phenomenological relaxation-time ansatz.

## V. MICROELECTRONICS

Because of the diversified nature of the service programs, it has become customary to report on only a few of the current programs in each of the major areas within the microelectronics program. In order to provide a broader view of the overall activities, at least on an occasional basis, we have chosen to summarize here all (or nearly all) of our current service commitments.

The mask-making area produces about 100 masks per month, and approximately 10 to 20 masks are employed in the microelectronics programs while much of the remainder is supplied to groups involved in surface wave acoustics, LSI, and materials research. The quality of delivered masks has improved considerably as a result of an intense investigation during the last few months into the causes of mask defects. The yield of high-resolution masks continues to be low primarily because of contamination problems in the mask-making area.

Current major service programs in the semiconductor area include:

- (a) Semiconductor structures for the surface wave acoustics program.
- (b) Double-sided semiconductor devices for nuclear particle detectors.
- (c) Photodiode arrays for the Educational Technology Program.
- (d) Large silicon devices for an optoelectronics sensor program.
- (e) Several types of silicon devices for the EBS (electron beam semiconductors) program.
- (f) Silicon wafers with various diffusions for the LSI program.
- (g) Microwave devices with special geometry.

Minor programs include:

- (a) Special devices or structures for several unrelated programs.
- (b) Silicon dioxide deposition for the materials research group.
- (c) Assorted devices for an in-house stock of parts for hybrid programs.

Present programs in the thin-film area include:

- (a) High-quality aluminum-silicon alloy film deposition on silicon wafers for the LSI program.
- (b) Electron beam film evaporation in support of the surface wave acoustic program.
- (c) Thin-film substrates for a 2-GHz transistor amplifier.
- (d) Thin-film substrates for a 3-MHz limiter, 30-MHz limiter, feedback amplifier, and several other hybrid circuits.

- (e) Preparation of transition metal oxide films for metal-insulator transition studies.
- (f) Thin-film structures for microwave circulators.

In addition, the thin-film area provides routine processing of about 100 items per month.

The bonding and assembly area has fabricated about 50 prototype hybrid circuits during this quarter, apart from the assembly and packaging of devices relating to the programs listed under the semiconductor area. The bonding area also undertakes about 15 to 20 separate and special tasks per month for other groups.

The throughput time for hybrid circuits presently averages about 3 months, and at least 6 weeks of this time is the delay associated with the procurement of devices or parts from industry. When the parts are all fabricated in-house (as, for example, in the case of the photo-diode array for the Educational Technology Program), the throughput time, which includes some development effort, is 28 days.

The research and development programs have been less active recently as a result of increased service commitments. Air-gap crossovers for monolithic integrated circuit metalization has received some attention and is being designed into a digital diode matrix. The laser scanner for testing integrated circuits is being used as a working test instrument for service programs, and no further development is planned.



# REPORTS ON SOLID STATE RESEARCH

15 November 1971 through 15 February 1972

## PUBLISHED REPORTS

		<u>Journal Articles*</u>	
<u>JA No.</u>			
3775	Partial Pressures in the Cd-Te and Zn-Te Systems	R. F. Brebrick	J. Electrochem. Soc. <u>118</u> , 2014 (1971), DDC AD-737160
3786	Luminescence of EuTe and Other Europium Chalcogenides	D. Hulin <sup>†</sup> J. Hanus <sup>†</sup> C. B. A La Guillaume <sup>†</sup> T. B. Reed	Solid State Commun. <u>8</u> , 1525 (1970)
3797	Conductivity Studies in Europium Oxide	M. R. Oliver J. O. Dimmock A. L. McWhorter T. B. Reed	Phys. Rev. B <u>5</u> , 1078 (1972), DDC AD-737932
3885	Accurate X-Ray Diffraction Measurements at High Pressures: Volume Compression of TiO <sub>x</sub>	M. D. Banus M. C. Lavine	High Temperatures-High Pressures <u>2</u> , 671 (1970), DDC AD-736303
3887	High Pressure Synthesis of (ABX <sub>3</sub> ) (AX) <sub>n</sub> Compounds	J. A. Kafalas J. M. Longo <sup>†</sup>	J. Solid State Chem. <u>4</u> , 55 (1972), DDC AD-737940
3894	High Apparent Mobility in Inhomogeneous Semiconductors	C. M. Wolfe G. E. Stillman J. A. Rossi	J. Electrochem. Soc. <u>119</u> , 250 (1972), DDC AD-738715
3899	Exciton Bands in Antiferromagnetic Cr <sub>2</sub> O <sub>3</sub>	R. M. Macfarlane <sup>†</sup> J. W. Allen	Phys. Rev. B <u>4</u> , 3054 (1971)
3908	Spin-Wave Theory of Two-Magnon Raman Scattering in a Two-Dimensional Antiferromagnet	S. R. Chinn R. W. Davies H. J. Zeiger	Phys. Rev. B <u>4</u> , 4017 (1971), DDC AD-737168
3913A	Precision Verification of Effective Mass Theory for Shallow Donors in GaAs	G. E. Stillman D. M. Larsen C. M. Wolfe R. C. Brandt <sup>†</sup>	Solid State Commun. <u>9</u> , 2245 (1971)
3917	Comment on the Magnetic Properties of Several Indium Thiospinels	J. B. Goodenough	J. Solid State Chem. <u>4</u> , 292 (1972), DDC AD-738716

---

\* Reprints available.

<sup>†</sup> Author not at Lincoln Laboratory.

JA No.

- |      |  |  |  |
|------|--|--|--|
| 3940 | Raman Scattering from Europium Chalcogenides                                   | R. K. Ray*<br>J. C. Tsang*<br>M. S. Dresselhaus<br>R. L. Aggarwal*<br>T. B. Reed | Phys. Letters <u>37A</u> , 129 (1971)                        |
| 3948 | Optical Observation of Stress-Induced Spin Flop in $\text{Cr}_2\text{O}_3$     | J. W. Allen  | Phys. Rev. Letters <u>27</u> , 1526 (1971),<br>DDC AD-737163 |
| 3965 | Optically Pumped Room-Temperature $\text{In}_x\text{Ga}_{1-x}\text{As}$ Lasers | J. A. Rossi<br>S. R. Chinn<br>A. Mooradian                                       | Appl. Phys. Letters <u>20</u> , 84 (1972),<br>DDC AD-737941  |
| 3975 | Near-Resonance Spin-Flip Raman Scattering in Indium Antimonide                 | S. R. J. Brueck<br>A. Mooradian  | Phys. Rev. Letters <u>28</u> , 161 (1972),<br>DDC AD-738726  |

Meeting Speeches
MS No.

- |      |  |  |   |
|------|--|--|---|
| 2964 | Magneto-Optical Properties of the Eu-Chalcogenides   | J. O. Dimmock  | The Physics of Opto-Electronic Materials, W.A. Albers, Jr., Ed. (Plenum, New York, 1971), pp. 255-271, DDC AD-737950  |
| 2992 | Varied Roles of the Outer d Electrons  | J. B. Goodenough   | Chap. III in <u>Proceedings of the Robert A. Welch Foundation Conference on Chemical Research XIV, Solid State Chemistry</u> , Houston, Texas, 9-11 November 1970, W. O. Milligan, Ed. (The Robert A. Welch Foundation, Houston, 1971), p. 75 |
| 3067 | Polaron Morphologies in Vanadium Oxides  | J. B. Goodenough   | <u>Conduction in Low-Mobility Materials</u> , N. Klein, D. S. Tannhauser and M. Pollak, Eds. (Taylor & Francis Ltd., London, 1971), p. 87   |
| 3144 | Materials and Processing Techniques for the Fabrication of High Quality Millimeter Wave Diodes | B. J. Clifton<br>W. T. Lindley<br>R. W. Chick<br>R. A. Cohen | Proc. Third Biennial Cornell Electrical Engineering Conference, Cornell University, Ithaca, 17-19 August 1971, p. 463   |
| 3192 | Tunable Infrared Lasers and Their Applications   | P. L. Kelley<br>E. D. Hinkley<br>A. Mooradian                | NEREM Record <u>13</u> , Pt. 1, 221 (1971),<br>DDC AD-738713  |

---

\* Author not at Lincoln Laboratory.

## UNPUBLISHED REPORTS

Journal Articles

<u>JA No.</u>			
3857	Comment on "Observation of Nonextremal Fermi Surface Orbits in Bulk Bismuth" — Author's Reply	V. E. Henrich	Accepted by Phys. Rev.
3880	Influence of Atomic Vacancies on the Properties of Transition-Metal Oxides: I. $\text{TiO}_x$ and $\text{VO}_x$	J. B. Goodenough	Accepted by Phys. Rev. B
3889	Electrical and Magnetic Properties of 'TiO' and 'VO'	M. D. Banus T. B. Reed A. J. Strauss	Accepted by Phys. Rev. B
3892	Shubnikov-de Haas Measurements in $\text{Pb}_{1-x}\text{Sn}_x\text{Se}$	J. Melngailis T. C. Harman W. C. Kernan	Accepted by Phys. Rev. B
3900	The Heats of Transformation of the High-Pressure Orthorhombic Modification of Indium Antimonide	A. K. Jena* M. B. Bever* M. D. Banus	Accepted by Met. Trans.
3901	Thermal Brillouin Scattering in Cadmium Sulfide: Velocity and Attenuation of Sound; Acoustoelectric Effects	A. S. Pine	Accepted by Phys. Rev. B
3902	Resonance Brillouin Scattering in Cadmium Sulfide	A. S. Pine	Accepted by Phys. Rev. B
3911A	Superconductivity in Cubic and Monoclinic "TiO"	T. B. Reed M. D. Banus M. Sjöstrand* P. H. Keesom*	Accepted by J. Appl. Phys.
3929	Effect of Pressures to 50 kbar on the Magnetic Behavior of MnP	M. D. Banus	Accepted by J. Solid State Chem.
3939	Study of the Optical de Haas-Shubnikov Effect	F. P. Missell* M. S. Dresselhaus	Accepted by Phys. Rev. B
3943A	Non-T Donor Levels and Kinetics of Electron Transfer in n-Type CdTe	G. W. Iseler J. A. Kafalas A. J. Strauss H. F. MacMillan* R. H. Bube*	Accepted by Solid State Commun.

---

\* Author not at Lincoln Laboratory.

## JA No.

3957	The Pressure Dependence of the Carrier Concentrations in P-Type Alloys of $\text{Hg}_{1-x}\text{CdTe}$ at 4.2°K and 77°K	C. T. Elliott* J. Melngailis T. C. Harman J. A. Kafalas W. C. Kernan	Accepted by Phys. Rev.
3967	Sealed Crucible Technique for Thermal Analysis of Volatile Compounds up to 2500°C: Melting Points of EuO, EuS, EuSe and EuTe	T. B. Reed R. E. Fahey A. J. Strauss	Accepted by J. Crystal Growth
3969	Energy Bands in $\text{TX}_2$ Compounds with Pyrite, Marcasite, and Arsenopyrite Structures	J. B. Goodenough	Accepted by J. Solid State Chem.
3971	Raman Scattering in Paratellurite: $\text{TeO}_2$	A. S. Pine G. Dresselhaus	Accepted by Phys. Rev.
3988	Single Crystal Growth of $\text{Hg}_{1-x}\text{Cd}_x\text{Te}$	T. C. Harman	Accepted by J. Electron. Mater.
3992	Preparation and Structure of a Pyrochlore and Perovskite in the $\text{BiRhO}_{3+x}$ System	J. M. Longo* P. M. Raccach* J. A. Kafalas J. W. Pierce	Accepted by Mater. Res. Bull.
MS-3090	Influence of Madelung Energy and Covalency on Structure of $\text{A}^+\text{B}^{5+}\text{O}_3$ Compounds	J. A. Kafalas	Accepted by Proc. NBS 5th Materials Research Symposium, Solid State Chemistry, Gaithersburg, Maryland, 18-21 October 1971
MS-3120	Preparation and Structure of a Pyrochlore and Perovskite in the $\text{BiRhO}_{3+x}$ System	J. M. Longo* P. M. Raccach* J. A. Kafalas J. W. Pierce	

## Meeting Speeches†

## MS No.

2951D	Localized vs Itinerant Electrons	J. B. Goodenough	Winter School in Solid State Chemistry, Indian Institute of Technology, Kanpur, India, 22 November – 10 December 1971
3032A	Polaron Self-Energy Effects on Higher Landau Levels in InSb	E. J. Johnson	Seminar, Naval Research Laboratory, Washington, D.C., 31 January 1972
3152B	Acoustical and Optical Activity in Crystals	A. S. Pine	Seminar, Yeshiva University, New York, 9 February 1972

\* Author not at Lincoln Laboratory.

† Titles of Meeting Speeches are listed for information only. No copies are available for distribution.



# Reports

## MS No.

3182	High Spin-Low Spin and Structural Transition in $\text{LaCoO}_3$	R. A. Bari	17th Annual Conference on Magnetism and Magnetic Materials, Chicago, 16-19 November 1971
3186	Recent Topics in Two-Magnon Optical Raman Scattering	S. R. Chinn R. W. Davies H. J. Zeiger	
3187	Electronic Raman Scattering in $\text{FeF}_2$	S. R. Chinn H. J. Zeiger	
3231	Elastic Constants, Compressibilities and Debye Temperatures of the Eu-Chalcogenides	Y. Shapira* T. B. Reed	
3222	Energy Bands in Arsenic	R. W. Brodersen G. Dresselhaus M. S. Dresselhaus	American Physical Society Meeting, Cambridge, Massachusetts, 27-29 December 1971
3223	Optical Properties of Graphite	L. G. Johnson G. Dresselhaus	
3224	Reflectivity and Optical Constants of $\text{SnO}_2$	C. L. Rieck M. S. Dresselhaus W. Scouler C. G. Fonstad*	
3228	Raman Scattering in the Europium Chalcogenides	R. K. Ray* J. C. Tsang* R. Aggarwal M. S. Dresselhaus T. B. Reed	
3229	Infrared Laser Determination of Effective Mass in GaAs-InAs Alloys	J. Waldman H. R. Fetterman P. E. Tannenwald C. M. Wolfe	
3242	Exploring Semiconductor Impurity Properties by Magnetospectroscopy of Shallow Donors	D. M. Larsen	

\* Author not at Lincoln Laboratory.

# ORGANIZATION

## SOLID STATE DIVISION

A. L. McWhorter, *Head*  
P. E. Tannenwald, *Associate Head*  
C. R. Grant, *Assistant*

### QUANTUM ELECTRONICS

A. Mooradian, *Leader*  
P. L. Kelley, *Associate Leader*

Brueck, S. R. J.	Johnson, E. J.
Burke, J. W.	Moulton, P. F.*
Chinn, S. R.	Pine, A. S.
Eng, R. S.	Rossi, J. A.
Hancock, R. C.	

### ELECTRONIC MATERIALS

J. B. Goodenough, *Leader*  
A. J. Strauss, *Associate Leader*

Anderson, C. H., Jr.	LaFleur, W. J.
Batson, D. A.	Lavine, M. C.†
Button, M. J.	Mastromattei, E. L.
Coppola, A. J.	Mikkelsen, J. C., Jr.
Delaney, E. J.	Mroczkowski, I. H.
Fahey, R. E.	Owens, E. B.
Fan, J. C. C.	Pantano, J. W.
Finn, M. C.	Pierce, J. W.
Hong, H. Y-P	Plonko, M. C.
Hsieh, J. J.	Reed, T. B.
Iseler, G. W.	Tracy, D. M.
Kafalas, J. A.	

### MICROELECTRONICS

R. E. McMahon, *Leader*

Bachner, F. J.	Gray, R. V.
Beatrice, P. A.	McGonagle, W. H.
Clough, T. F.	Mountain, R. W.
Cohen, R. A.	Pichler, H. H.
Durant, G. L.	Smythe, D. L.
Grant, L. L.	Wilde, R. E.

### SOLID STATE PHYSICS

J. G. Mavroides, *Co-Leader*  
H. J. Zeiger, *Co-Leader*  
G. B. Wright, *Assistant Leader (LOA)*

Allen, J. W.	Henrich, V. E.
Barch, W. E.	Johnson, L.*
Blum, F. A., Jr.	Kernan, W. C.
Brodersen, R. W.*	Kolesar, D. F.
Davies, R. W.	Korn, D. M.
DeFeo, W. E.	Larsen, D. M.
Dresselhaus, G. F.	Melngailis, J.
Dresselhaus, M. S.†	Menyuk, N.
Dwight, K., Jr.	Nill, K. W.
Feldman, B.	Parker, C. D.
Fetterman, H.	Seccombe, D.*
Groves, S. H.	

### APPLIED PHYSICS

I. Melngailis, *Leader*  
A. G. Foyt, *Assistant Leader*  
T. C. Harman, *Assistant Leader*

Belanger, L. J.	McBride, W. F.
Calawa, A. R.	Murphy, R. A.
Carter, F. B.	Orphanos, W. G.
DeMeo, N.	Paladino, A. E.
Donnelly, J. P.	Palm, Barbara J.†
Ferrante, G. A.	Ralston, R. W.
Hurwitz, C. E.	Spears, D. L.
Krohn, L., Jr.	Stillman, G. E.
Landon, Susan N.	Ward, J. H. R., III
Leonburger, F.*	Wolfe, C. M.
Lincoln, G. A.	Youtz, P.
Lindley, W. T.	

### MICROSOUND

E. Stern, *Leader*

Alusow, J. A.	Chen, F.
Brogan, W. T.	Smith, H. I.
Burke, B. E.	Williamson, R.

---

\* Research Assistant

† Part Time

## I. SOLID STATE DEVICE RESEARCH

### A. DETECTIVITY MEASUREMENTS ON GUARDED InSb n-p JUNCTIONS FABRICATED USING PROTON BOMBARDMENT

Infrared detectivity as a function of wavelength was measured for the InSb n-p junction photodiodes with annular guard-ring field plates which were described in a previous report.<sup>1</sup> To do this, the relative spectral response, blackbody responsivity, noise, and quantum efficiency of these devices were measured with the diode at 77°K. For these measurements, the field-plate voltage was adjusted to give the highest zero-bias device resistance. In addition, the diode voltage was adjusted using a high-resistance (100 megohm) metal-film resistor and a variable power supply. The diode voltage was measured using an electrometer, and kept to within  $\pm 1$  mV of zero voltage.

Background radiation which was incident on the device was varied using different cooled apertures between the diode and the (295°K) room-temperature background. The size of these apertures was varied to give backgrounds varying from a 90° FOV, 295°K background to a completely shielded (77°K) background.

The relative response measured as above was found to be independent of background. Also, the blackbody responsivity was found to be essentially independent of background, although in some cases a slight increase in responsivity was observed as the background was reduced. However, the noise was found to be a strong function of the background radiation, decreasing as the background was reduced. For the completely shielded case, the biasing resistor and power supply were omitted, since the diode voltage was within  $\pm 1$  mV of zero voltage without them.

Detectivity-vs-wavelength curves were calculated for these devices using the responsivity measured with the 20° FOV aperture, and the noise measured in the completely shielded situation. It should be noted that this calculation should slightly underestimate the detectivity in the reduced background situation, since the responsivity was found to increase slightly as the background was reduced.

The detectivity-vs-wavelength curve for the diode with the largest detectivity is shown in Fig. I-1; also shown is the quantum efficiency (QE) at the wavelength of peak response. For this device, the resistance at zero bias was  $\sim 20$  megohms, as determined using DC current-voltage measurements. It should be noted that the measured detectivity value of  $2.75 \times 10^{12}$  cm $\sqrt{\text{Hz}}$ /W is close to but somewhat less than the value of  $4 \times 10^{12}$  cm $\sqrt{\text{Hz}}$ /W determined by the device Johnson noise and quantum efficiency.

A. G. Foyt      W. T. Lindley  
C. E. Hurwitz   J. P. Donnelly

### B. InSb p-n JUNCTION PHOTODIODES FABRICATED BY Zn<sup>+</sup> ION IMPLANTATION

High-quality planar p-n junction photodiodes have been fabricated in InSb by the implantation of 400-kV Zn ions into n-type InSb.

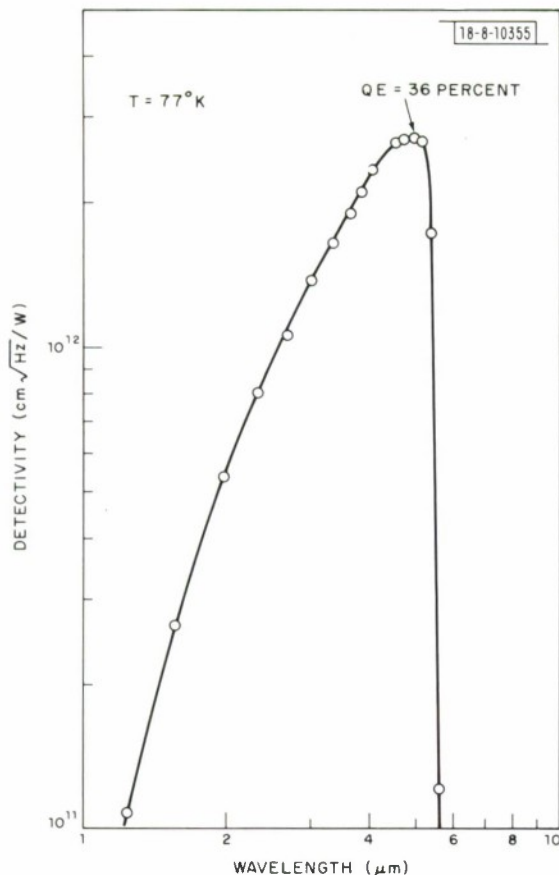


Fig. I-1. Detectivity vs wavelength for 20-mil-diameter InSb photodiode fabricated using proton bombardment to create n-type layer.

Prior to implantation, each sample was coated with thin ( $\sim 1000 \text{ \AA}$ ) sputtered  $\text{SiO}_2$  to protect the sample surface. The implantations were done with the samples at room temperature using a 400-kV  $\text{Zn}^+$  ion current of  $10^{-8} \text{ A/cm}^2$  to give a total ion dose of  $\sim 5 \times 10^{13} / \text{cm}^2$ . Each sample was then annealed at  $350^{\circ}\text{C}$  in a  $\text{N}_2$  atmosphere. The  $\text{SiO}_2$  layer was then removed, a thin ( $700 \text{ \AA}$ ) layer of InSb removed, and the sample recoated with a pyrolytic SiON layer to stabilize the surface.

Zero-bias resistances of 1 to 3 megohms at  $77^{\circ}\text{K}$  have been shown by 20-mil-diameter circular planar diodes made in this way. In reduced background, the peak detectivity of these devices is  $\sim 10^{12} \text{ cm} \sqrt{\text{Hz/W}}$  at  $5.3 \mu\text{m}$ . The quantum efficiencies of these diodes are high,  $\sim 60$  percent at  $5.3 \mu\text{m}$  for devices with no antireflection coating. In addition, the quantum efficiency remains high (over 40 percent) from the peak wavelength ( $5.3 \mu\text{m}$ ) to wavelengths as short as  $1 \mu\text{m}$ .

C. E. Hurwitz    J. P. Donnelly  
A. G. Foyt        W. T. Lindley

### C. K-BAND BaAs IMPATT DIODES

A CW oscillator power output of 380 mW at 28 GHz with an efficiency of 6.8 percent has been achieved with an epitaxial GaAs Schottky barrier IMPATT diode having an active device diameter of 2 mils. Also, 275 mW of CW power at 32 GHz with an efficiency of 7.8 percent have been



produced by a p-n junction device also having a 2-mil junction diameter. This device produced about 13 dB of small signal gain at comparable frequencies when operated as an amplifier.

A sketch of the epitaxial Schottky barrier device is shown in Fig. I-2. This device is fabricated on an n-n<sup>+</sup> epitaxial GaAs substrate, with electron densities in the epitaxial layer from  $5$  to  $9 \times 10^{16}$  electrons/cm<sup>3</sup>. The first step in the device fabrication is to etch a 3.5- $\mu$ m-deep grid of channels into the epitaxial side of a thick (~15 mils) wafer of GaAs using photolithographic techniques. A 0.2- $\mu$ m layer of platinum is then plated over the entire epitaxial surface, which forms the active Schottky barrier. A thick (4 to 5 mils) layer of copper is then plated onto the platinum to ensure an intimate thermal contact with the heat-producing region of the diode. Measurements of the thermal resistance of mounted devices by various means have yielded thermal resistances near the theoretically predicted minimum.

The thick layer of GaAs is then lapped and polished from the side opposite the copper heat sink until only a thin (3  $\mu$ m) layer of GaAs remains, as indicated by the channels described above. Chrome-gold back contacts (3  $\mu$ m thick, 1.5 to 3 mils in diameter) are then patterned onto the wafer. The sample is then bombarded with 400-kV protons which penetrate the 3  $\mu$ m of GaAs. The Cr-Au back contacts are sufficiently thick to completely shield the material under them from the proton beam. The bombarded GaAs, which is converted to semi-insulating material, serves to isolate device areas and, most importantly, to suppress edge breakdown. Also, this process affords both ease and precision in the delineation of device areas. The bombarded wafer is then diced on a multi-cut string saw, and packaged.

The p-n junctions are fabricated by zinc implantation. Thus far, this has only been done on a wafer of bulk GaAs, with the results mentioned above. The heat-sinking and guarding techniques employed were similar to those already described. Contact to the p-region is in this case made by a plated layer of platinum.

The ultimate objective of this effort is to provide the active elements of the amplifier for the K-band transmitter in the LES-8 and -9 satellites. To this end, the diodes must be capable of handling power levels on the order of  $\frac{1}{4}$  W at 36 to 38 GHz for several years. An immediate objective is to adjust the external microwave circuitry and/or the electron density in the active layer in order to obtain operation in the desired frequency range. In addition, various mechanisms (e.g., alloying, diffusion effects, breakdown of the proton guarding) which could cause failure after long continuous use are being examined, and life testing of the diodes is being started.

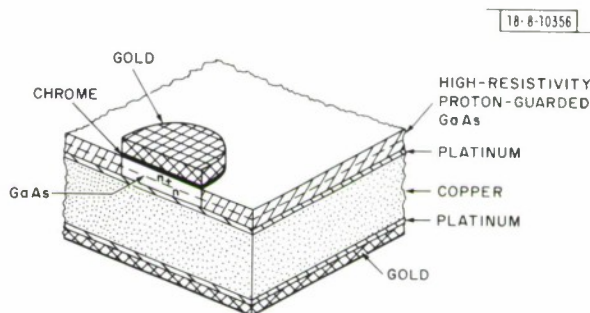


Fig. I-2. Section of Schottky barrier epitaxial IMPATT diode.

R. A. Murphy      D. M. Snider\*  
W. T. Lindley      A. G. Foyt  
D. F. Peterson\*

\* Group 63.

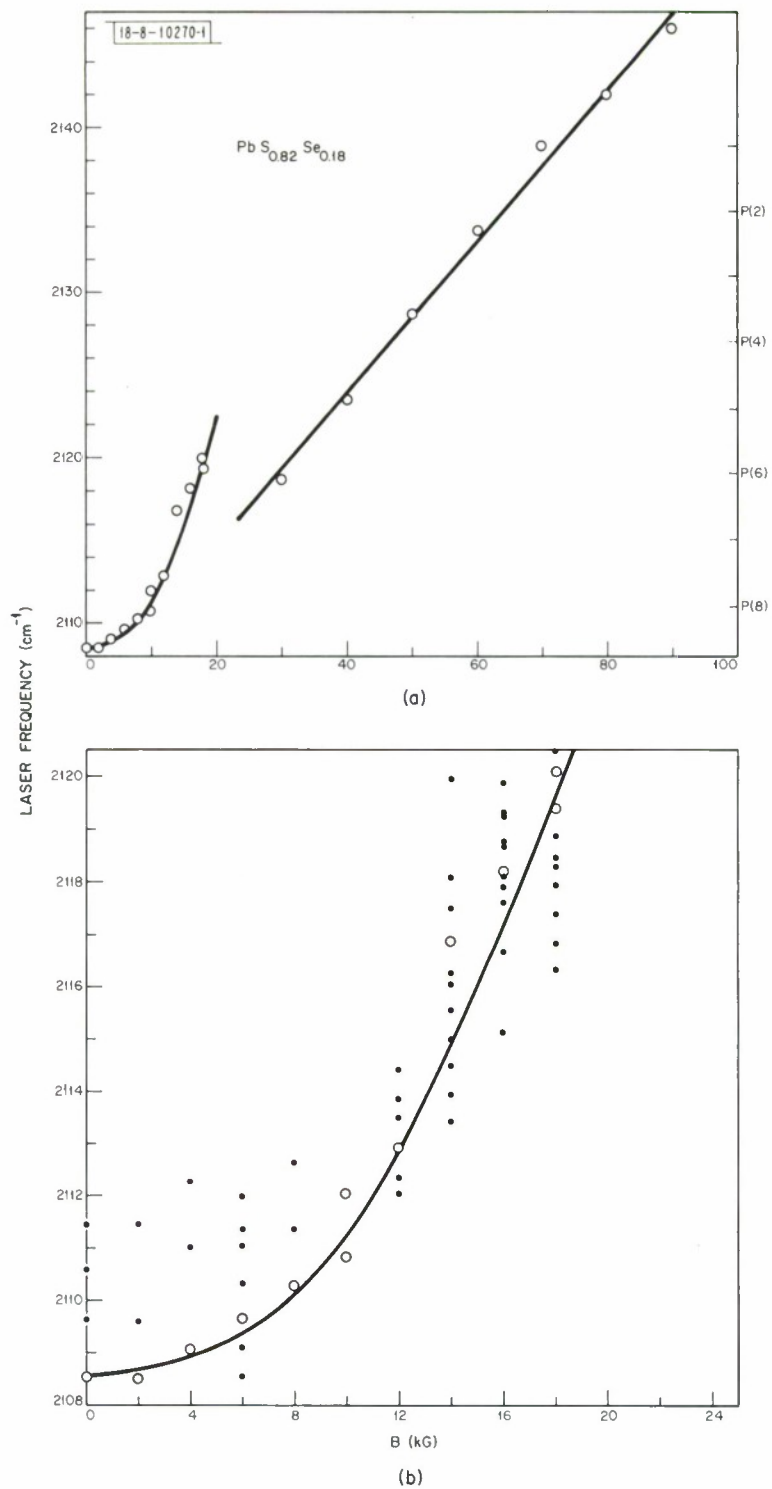


Fig. 1-3. Gross frequency-tuning characteristics of  $\text{PbS}_{0.82}\text{Se}_{0.18}$  laser: (a) general magnetic-field characteristics, (b) detailed low-field-magnetic frequencies.

#### D. MAGNETIC-FIELD-TUNED PbSSe LASERS FOR HIGH-RESOLUTION SPECTROSCOPY

Magnetic-field tuning has been used to significantly extend the tuning capabilities of PbSSe semiconductor lasers. In addition to achieving an increased tuning range<sup>2</sup> (~2 percent of the laser energy), we have also studied the details of the continuous Fabry-Perot mode fine tuning produced by the magnetic field. The semiconductor lasers of  $\text{PbS}_{1-x}\text{Se}_x$  were operated CW at 4.7 and 5.4  $\mu\text{m}$  for  $x = 0.18$  and 0.39, respectively. The devices were mounted on the cold finger of a liquid helium dewar at 10° to 12°K with the magnetic field applied parallel to the current flow using either a conventional electromagnet providing 18.5 kG or a 100-kG superconducting solenoid. The output power under typical operating conditions occurred in two or three closely spaced ( $\sim 0.6 \text{ cm}^{-1}$ ) strong modes with  $\geq 10 \mu\text{W}$  in each mode. The gross tuning of the center of the mode pattern was measured using a double-grating spectrometer with a resolution  $\leq 0.1 \text{ cm}^{-1}$ . Measurement of the fine-tuning rate of the individual modes was made by tuning the mode through a gas absorption of known width. Accurate determination of this fine-tuning rate using the spectrometer was not possible since the total fine-tuning range of a single mode tuned with magnetic field was quite small (0.1 to 0.2  $\text{cm}^{-1}$ ).

Figure I-3(a) illustrates the gross magnetic-field tuning of a 4.7- $\mu\text{m}$   $\text{PbS}_{0.82}\text{Se}_{0.18}$  laser operating CW near 10°K at a current of about 50 percent above laser threshold. The points locate the strongest operating mode which is close to the center of the spontaneous gain. The two branches are associated with different electronic transitions between the spin-split Landau levels of the conduction and valence bands. Very similar behavior has been observed in other semiconductor lasers such as PbTe, PbSe (Ref. 3), and InSb (Ref. 4). The CW output power of this device was substantially unaffected by the large magnetic field up to the largest field employed of 90 kG. Presumably, the tuning could be extended considerably above the values of Fig. I-3(a) if the magnetic fields were available. Using this laser, we have obtained high-resolution spectra of several of the P-branch lines of CO between P(8) and P(3). The locations of these absorption lines are indicated on the right-hand margin. Spectra were obtained by adjusting the magnetic field to obtain a mode near the absorption and then current-tuning this mode through the absorption frequency. While the mode could be fine-tuned with the magnetic field, our detailed measurements reveal several difficulties with this procedure as will be described below. The locations of the laser modes present up to 18 kG are shown in Fig. I-3(b). It is difficult to follow the position of a mode with field since the range of a mode is usually only 3 to 5 kG and the frequency change over this interval is 0.1  $\text{cm}^{-1}$  or less. While this rapid mode hopping may appear to be troublesome, the multitude of operating modes (up to 11 in this case) permits nearly complete coverage of the entire frequency range between 2108 and 2146  $\text{cm}^{-1}$ .

Measurement of the fine-tuning rate of the laser modes was difficult because of the narrow tuning range of individual modes. It was necessary to use the gas absorption technique described below. The output mode of a  $\text{PbS}_{0.82}\text{Se}_{0.18}$  laser operating near 2115  $\text{cm}^{-1}$  was transmitted through a 10-cm gas cell containing 0.05 torr of CO gas at room temperature. The laser mode could be tuned through the P(7) absorption line of the gas which at this pressure has the Gaussian Doppler profile with a Doppler width of 148 MHz (Ref. 2). Measuring the magnetic-field increment required to tune through the Doppler width gives the magnetic-field fine-tuning rate. Since the mode frequency can be independently controlled by the diode current, it was possible to

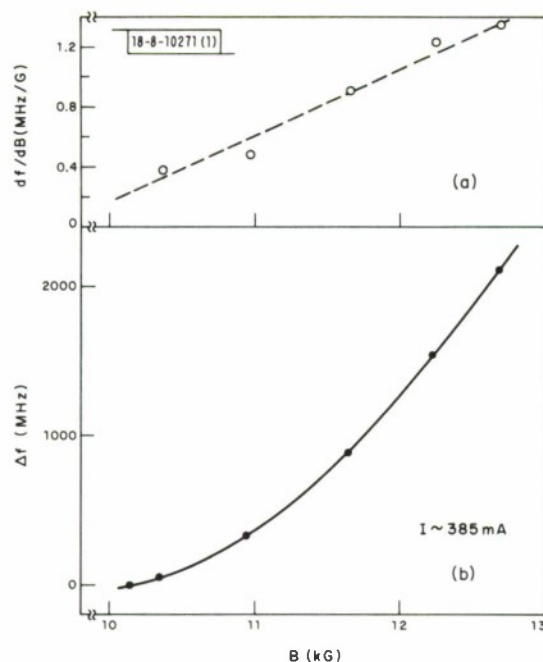


Fig.1-4. Fine-tuning characteristics of  $\text{PbS}_{0.82}\text{Se}_{0.18}$  laser mode showing (a) rapid change in tuning rate  $df/dB$  with field, and (b) field dependence of mode frequency (see text).

change the magnetic field at which the P(7) absorption occurred. Hence, the fine-tuning rate could be measured at several magnetic fields over the tuning range of the mode. The results of this procedure are shown in Fig.1-4(a). The tuning rate  $df/dB$  changes by almost a factor of 4 over the narrow-field interval between 10 and 13 kG. Another technique which provided consistent results involved measuring the change in field necessary to reach the absorption line after a change in current. The current was calibrated in terms of frequency (243 MHz/mA) by current-tuning the mode through the same gas absorption. This procedure yielded the relative frequency calibration shown in Fig.1-4(b). The slope of this line gives a magnetic-field tuning rate in quite good agreement with that determined by measuring the width of the gas absorption. A nonlinear variation such as shown in Fig.1-4(b) severely complicates use of this tuning technique for high-resolution spectroscopy due to the difficulty in obtaining an accurate tuning calibration at all fields. The nonlinear behavior of  $df/dB$  may be less important at high fields where the variation of the energy gap with field [Fig.1-3(a)] becomes quite linear. However, detailed measurements of the tuning characteristics have not been made above  $\sim 17$  kG.

The magnetic-field tuning rate  $df/dB$  can be directly related to the magnetic-field dependent optical index  $n$ ,

$$\frac{1}{f} \frac{df}{dB} = - \frac{1}{n_{\text{eff}}} \frac{\partial n}{\partial B} \bigg|_f \quad (1-1)$$

Here,  $n_{\text{eff}} \approx 5.8$  is the effective index deduced from the mode spacing ( $0.57 \text{ cm}^{-1}$ ) and the laser length ( $0.15 \text{ cm}$ ). Mode pulling is neglected in Eq. (1-1) since the spontaneous width ( $\sim 5 \text{ cm}^{-1}$ ) is large compared with the cavity linewidth. Over the range from 10 to 13 kG in Fig.1-4(a-b),



the quantity  $\partial n / \partial B|_f$  changes from  $-0.4$  to  $-1.5 \times 10^{-7}/G$ . This is the first observation of a nonlinear variation of the mode frequency with magnetic field. In addition to severely limiting the usefulness of magnetic-field fine tuning of diode lasers, the nonlinear variation of the index with field may also have implications for other magnetic-field tuned lasers such as the low-field InSb spin-flip laser.

K. W. Nill      A. R. Calawa  
F. A. Blum    T. C. Harman

#### E. OPTICALLY PUMPED $Pb_{1-x}Ge_xTe$ AND $Pb_{1-x}Ge_xS$ LASERS

Laser emission has been observed in vapor-grown  $Pb_{1-x}Ge_xTe$  and  $Pb_{1-x}Ge_xS$  crystals optically pumped using a GaAs diode laser source. The results suggest that these materials are potentially useful for fabricating diode lasers at any desired wavelength in the 3.4- to 6.6- $\mu m$  range which is bounded by the shortest wavelength so far observed in  $Pb_{1-x}Ge_xS$  and the wavelength of PbTe lasers.

TABLE I-1 OPTICALLY PUMPED $Pb_{1-x}Ge_xTe$ AND $Pb_{1-x}Ge_xS$ LASERS						
Material	Sample Na.	Crystal Na.	Nominal Source Composition ( $x_s$ )	Temperature ( $^{\circ}K$ )	Wavelength ( $\mu m$ )	Threshold Pump Power (W)
$Pb_{1-x}Ge_xTe$	1T	VG-Bi-2	0.087	10	5.4	4.0
	2T	VG-Bi-2	0.087	10	5.4	2.0
	3T	MCVG	0.15	10	5.27	0.3
$Pb_{1-x}Ge_xS$	1S	1.5-2	0.015	10	3.40	5.0
	2S	1.5-2	0.015	10	3.42	3.0
	3S	1.5-2	0.015	10	3.43	1.5
	3S	1.5-2	0.015	40	3.33	3.5

The results on a number of  $Pb_{1-x}Ge_xTe$  and  $Pb_{1-x}Ge_xS$  samples are summarized in Table I-1. Emission spectra of a  $Pb_{1-x}Ge_xS$  laser (sample 2S) below and above threshold are shown in Fig. I-5. The crystals were grown at 800 $^{\circ}C$  by the vertical closed-tube vapor-growth technique previously used in growing other lead-chalcogenide crystals.<sup>5</sup> Crystal VG-Bi-2 was Bi-doped, whereas the other two crystals were undoped. The lowest annealing temperatures for crystals VG-Bi-2, MCVG and 1.5-2 were 350 $^{\circ}$ , 550 $^{\circ}$  and 500 $^{\circ}C$ , respectively. The lack of correlation between the nominal source composition and the laser output wavelength for crystals VG-Bi-2 and MCVG is possibly due to precipitated GeTe. The laser cavity, typically 300 $\mu m$  long, was either formed by cleaved or by as-grown (100) crystal faces. The crystals were mounted in front of the emitting face of the GaAs diode laser which was mounted on a heat sink in a variable temperature dewar, and the emission from the sample was observed in a direction perpendicular to the direction of the pump beam.

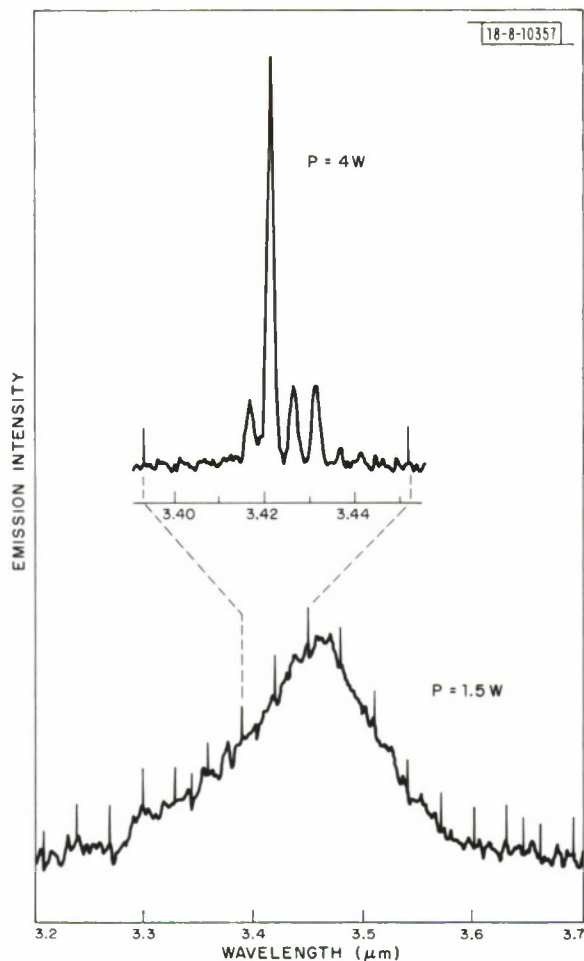


Fig.1-5. Emission spectra of optically pumped  $\text{Pb}_{1-x}\text{Ge}_x\text{S}$  laser (sample 2S) at  $10^\circ\text{K}$  below threshold for GoAs pump power of 1.5 W, and above threshold for pump power of 4 W. Laser linewidths are limited by resolution of LiF prism spectrometer used.

The laser threshold is given in Table 1-1 in terms of the total incident  $0.84\text{-}\mu\text{m}$  pump power, of which about one-half is reflected by the surface of the sample. The wavelengths of both  $\text{Pb}_{1-x}\text{Ge}_x\text{Te}$  and  $\text{Pb}_{1-x}\text{Ge}_x\text{S}$  lasers are very closely the same for crystals from the same vapor growth. For  $\text{Pb}_{1-x}\text{Ge}_x\text{Te}$ , the wavelength can be compared with the  $6.6\text{-}\mu\text{m}$  wavelength of PbTe lasers, and for  $\text{Pb}_{1-x}\text{Ge}_x\text{S}$  with the  $4.3\text{-}\mu\text{m}$  wavelength of PbS.

I. Melngailis  
T. C. Harman

#### REFERENCES

1. Solid State Research Report, Lincoln Laboratory, M.I.T. (1971:4), p. 1, DDC AD-736501.
2. *Ibid.* (1971:3), p. 7, DDC AD-731547.
3. J. F. Butler and A. R. Calawa in *Physics of Quantum Electronics*, P. L. Kelley, B. Lax and P. E. Tannenwald, Eds. (McGraw-Hill, New York, 1966), p. 458.
4. R. J. Phelan, Jr. and R. H. Rediker, *Proc. IEEE* **52**, 91 (1964).
5. I. Melngailis and T. C. Harman in *Semiconductors and Semimetals*, Vol. 5, R. K. Willardson and A. C. Beer, Eds. (Academic Press, New York, 1970), p. 111.

## II. QUANTUM ELECTRONICS

### A. DIODE-PUMPED $\text{In}_x\text{Ga}_{1-x}\text{As}$ AND $\text{InP}$ LASERS

Previous work on optically excited lasers has been extended to include diode-pumped samples of III-V semiconductor compounds. For example,  $\text{In}_x\text{Ga}_{1-x}\text{As}$  samples with previously measured thresholds of  $\sim 10^5 \text{ W/cm}^2$  at room temperature<sup>1</sup> should be capable of being excited by diode pumps whose intensities typically reach  $10^6 \text{ W/cm}^2$ . However, at the divergence angles typical for diode lasers, maintaining this pump intensity requires very good optical coupling to the sample and operation at power levels where the probability of diode failure is high. Fortunately, preliminary material characterization as well as other important information can be obtained by operating at low temperatures where the thresholds for laser operation are considerably reduced. We present data obtained on thresholds, operating-mode characteristics, and material parameters for several compositions of  $\text{In}_x\text{Ga}_{1-x}\text{As}$  and  $\text{InP}$  pumped by pulsed (200-nsec pulse length) GaAs diodes.

Some of the material properties for the samples used in this work are shown in Table II-1. All the samples were n-type. With exception of sample 2, the  $\text{In}_x\text{Ga}_{1-x}\text{As}$  samples were all epitaxially grown on conducting substrates and no further electrical characterization was attempted. The  $\text{InP}$  samples were polished from Czochralski-grown material. Table II-1 also shows the observed 20°K lasing wavelengths and the temperature range over which laser action has been achieved using diode pumps. The samples were prepared and mounted as described in Ref. 1.

TABLE II-1					
Sample No.	$N_D - N_A$ (300°K) ( $\text{cm}^{-3}$ )	$\mu$ (300°K) ( $\text{cm}^2/\text{V-sec}$ )	$\lambda_L$ (20°K) (Å)	Temperature (°K)	$n_e$
1 $\text{In}_{0.05}\text{Ga}_{0.95}\text{As}$	—	—	8710	20	9.6
2 $\text{In}_{0.05}\text{Ga}_{0.95}\text{As}$	$1.2 \times 10^{15}$	6100	8720	20	7.3
3 $\text{In}_{0.08}\text{Ga}_{0.92}\text{As}$	—	—	8940	20 to 200	$8.0 \pm 0.3$
4 $\text{In}_{0.14}\text{Ga}_{0.95}\text{As}$	—	—	9900	20	$9.2 \pm 0.3$
5 $\text{InP}$	$2.3 \times 10^{15}$	3200	8800	20 to 80	$10.6 \pm 0.4$

Figure II-1 shows typical 20°K laser emission spectra from each of the samples used in this work. The resolution used is shown in the upper trace by the small vertical lines. These curves were obtained using sample cavity lengths which match the diode pump width thus

## Section II

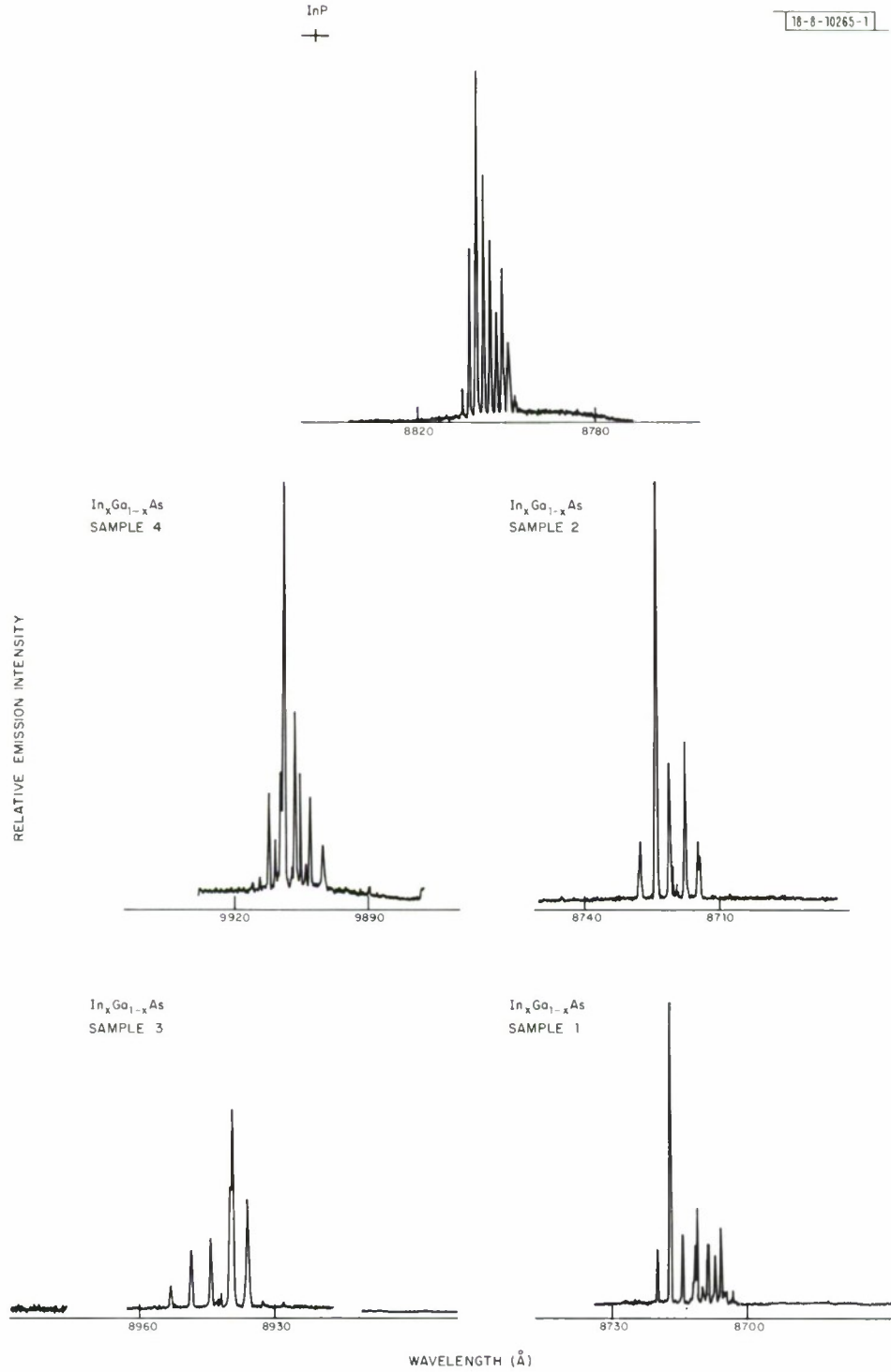


Fig.II-1. Laser emission spectra for  $\text{In}_x\text{Ga}_{1-x}\text{As}$  and InP lasers. For sample 1,  $x \approx 0.05$ ; sample 2,  $x \approx 0.05$ ; sample 3,  $x \approx 0.08$ ; and sample 4,  $x \approx 0.14$ .

excluding any shift of operating wavelength by a lossy or unexcited cavity.<sup>2</sup> As expected for the  $\text{In}_x\text{Ga}_{1-x}\text{As}$ , the wavelength at which the sample lases increases with InAs alloy content at a rate comparable to the shift of the bandgap with alloy composition.<sup>3</sup> Combining the data presented in Fig. II-1, the measured cavity lengths for the samples (accurate to  $\pm 2 \mu\text{m}$ ), and the standard axial mode spacing formula

$$\Delta\lambda = \frac{-\lambda^2}{2 \ln \left\{ 1 - \frac{\lambda}{n} \frac{dn}{d\lambda} \right\}} \equiv \frac{-\lambda^2}{2n_e L} \quad (\text{II-1})$$

we can easily compute  $n_e$ , an equivalent index of refraction which includes the effects of dispersion. This calculated value of  $n_e$  is shown as the last column entry in Table II-1.

The  $n_e$  results obtained in Table II-1 are checked by lasing samples of different cavity lengths for each composition, and the resulting variation in  $n_e$  is included as the  $\pm$  factor in the column. While the index of refraction and dispersion are known for GaAs and InAs, few data are available for the mixed alloy system. Relating the results presented in Table II-1 to existing work, we are thus comparing dispersion values for GaAs and InAs diodes to those of  $\text{In}_x\text{Ga}_{1-x}\text{As}$  platelets – a comparison which has definite limitations. By using typical values for  $n_e$  obtained from the literature for GaAs (Refs. 4 and 5) and InAs (Ref. 6) of 5.6 and 4.36, respectively, it is apparent that the values obtained in these experiments are significantly larger (cf. Table II-1). This trend is continued for the InP where direct comparison to previous and similar work<sup>7</sup> is possible ( $n_e \approx 7.7$ ). To our knowledge, these values of  $n_e$  are far larger than those previously observed for semiconductor lasers. The samples used here are n-type, and as such operate as lasers at photon energies higher than that which would occur from a heavily doped and compensated p-region of a diode made from the same starting material. Since operation at higher photon energies (or nearer the band edges) results in larger values for the dispersion,<sup>4</sup> this mechanism alone could account for these observations.

The temperature dependence of the lasing modes of these samples reveals some important features. As a typical case, we show in Fig. II-2 the temperature dependence of the emission from sample 3. Since the sample threshold increases with increasing temperature, fewer modes oscillate as the sample is warmed. As also shown in Fig. II-2, the individual mode widths begin to widen, progressing from  $\leq 0.2 \text{ \AA}$  (instrumental resolution) to 2 to 5  $\text{\AA}$  (far in excess of the resolution) as the temperature is raised.

To describe this mode broadening, we have two possibilities. First, one may postulate that at the higher temperatures several different transverse modes (belonging to the same axial mode) oscillate, thus apparently broadening the axial-mode line. The second, and more likely, explanation for this effect is that the sample active region undergoes a slight but rapid heating which is sufficient through the cavity resonance condition [Eq. II-(1)] to cause mode widening (i.e., a thermal or FM broadening). The heating may result directly from the increased pump intensity required to lase the samples at the higher temperatures. It has not been possible for us to conclusively identify the source of this broadening experimentally.

Figure II-3 illustrates the laser emission from a sample of InP lasing at 20°K. The upper ( $1.2 I_0$ ) and lower ( $I_0$ ) portions are the emission spectra run with different pump excitation intensities on the sample. At the lower excitation, a single set of Fabry-Perot modes is operating



## Section II

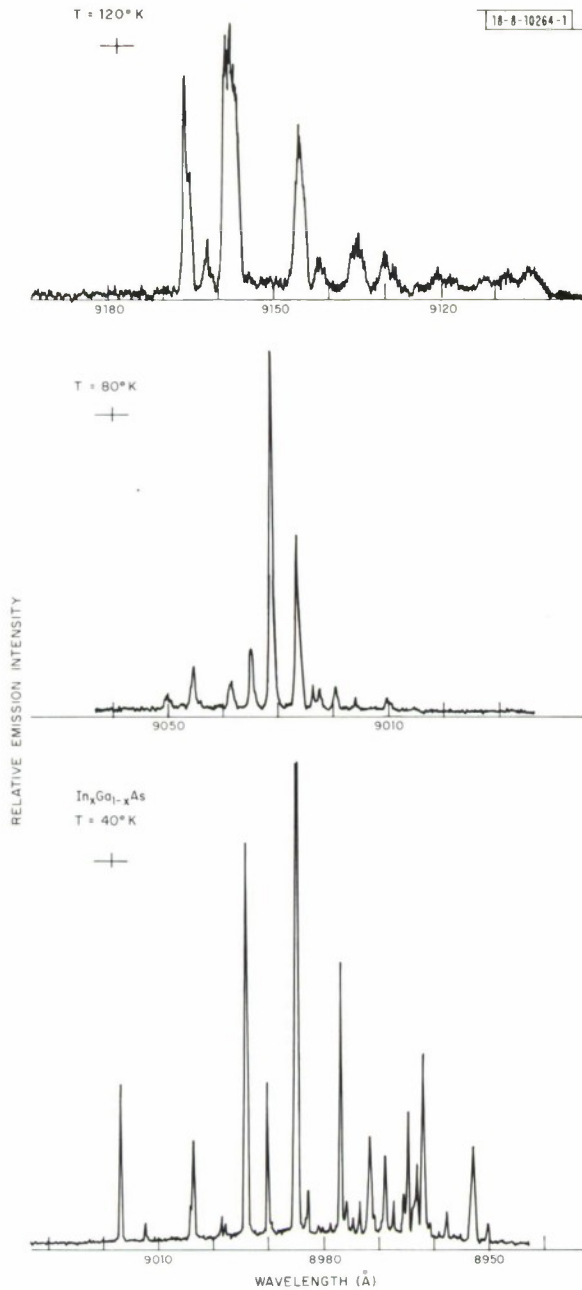


Fig.II-2.  $\text{In}_x\text{Ga}_{1-x}\text{As}$  ( $x \approx 0.08$ ) emission spectra as a function of temperature. Note increased broadening of individual modes as temperature is increased.

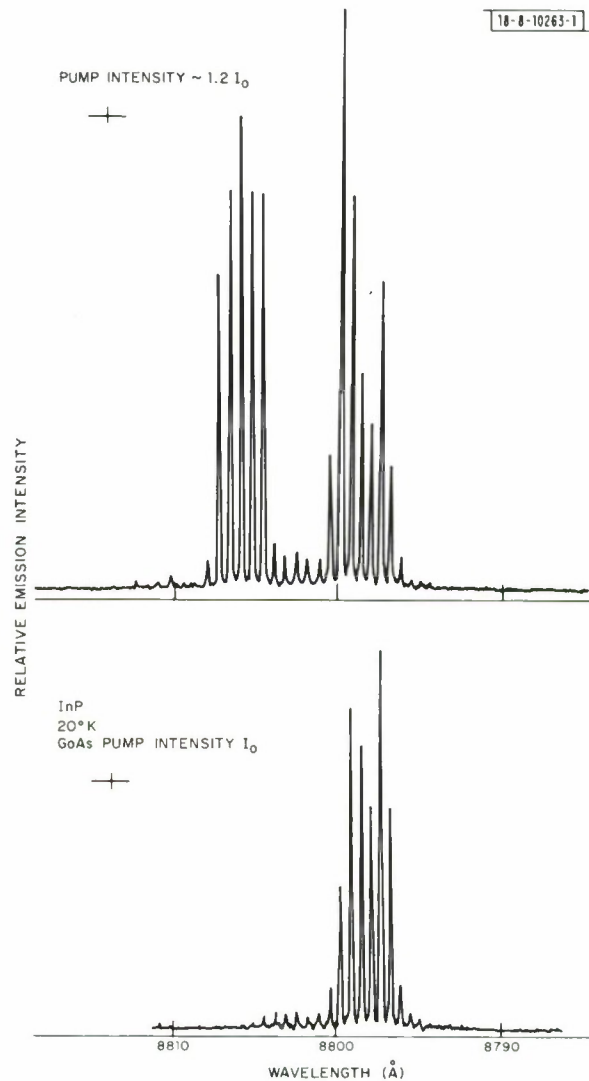


Fig.II-3. Emission spectra from InP as excitation intensity is increased from  $I_0$  to  $1.2 I_0$ .

and the mode spacing is consistent with the calculated spacing using the equivalent index  $n_e = 10.6$  (cf. Table II-1) and the measured cavity length ( $248 \mu\text{m}$ ). At the higher excitation level, another set of modes begins to oscillate and this set is similar to, but displaced from, the set of modes operating at the lower excitation intensity. We note that to the time resolution involved here, both mode sets are oscillating simultaneously; moving the detector  $\pm 50 \text{ nsec}$  substantially eliminates detection of both mode sets. We have observed this or similar behavior in every sample which has lased, so the results presented here are not unique to a particular cavity or composition. Such effects have also been observed in diodes<sup>8,9</sup> and possibly in electron-beam-pumped CdS (Ref. 10).

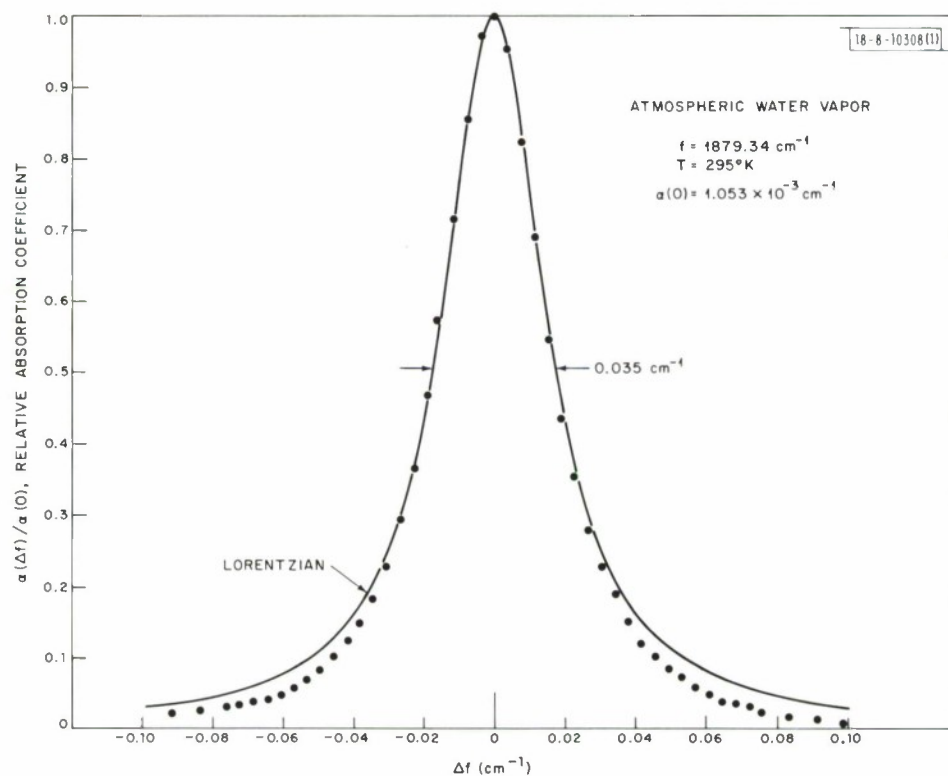
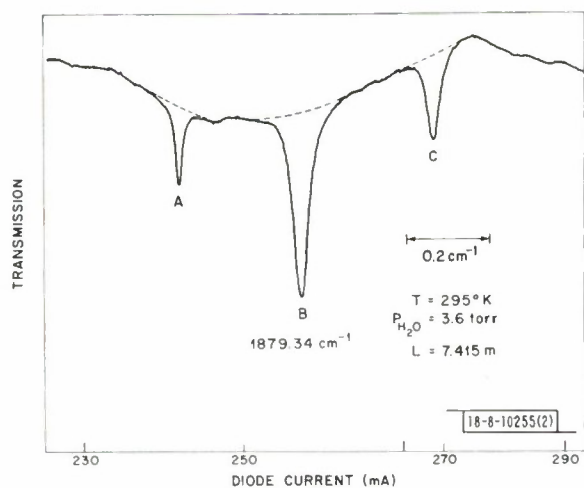
The appearance of two sets of modes so otherwise similar is suggestive of oscillation in two different transverse patterns. If the sample active region does support modes belonging to different transverse patterns, then it appears (cf. Fig. II-3) that the separation in wavelength between the different transverse sets is  $\sim 6 \text{ \AA}$ . This value is consistent with a predicted estimate for transverse mode separations obtained using the expression<sup>5</sup>  $\Delta\lambda = -\lambda^2 / 2\pi n_e \chi_\epsilon$  where, for  $\chi_\epsilon$  (the effective width of the guiding region), we use a value of  $\sim 20 \mu\text{m}$  and the value of  $n_e$  is taken from Table II-1. Although this latter expression was derived specifically for data pertaining to stripe geometry diodes, the similarity between the optically pumped cavity and the stripe geometry laser is evident. A direct measurement of the far-field radiation pattern is necessary to conclusively identify the different transverse modes. However, we note that if different transverse modes do oscillate, the spacing is determined by the focusing parameter  $\chi_\epsilon$ , and without the use of external optics, AR coatings, etc., simultaneous oscillation in several transverse modes will be difficult to suppress at power levels of practical interest.

J. A. Rossi  
S. R. Chinn  
C. M. Wolfe

## B. BROADBAND LASER EMISSION FROM OPTICALLY PUMPED $\text{PbS}_x\text{Se}_{1-x}$

Optically pumped lasers emitting between  $3.9$  and  $8.6 \mu\text{m}$  have been produced from  $\text{PbS}_x\text{Se}_{1-x}$  crystals of several alloy compositions. Multiaxial mode laser bandwidths of 10 percent of the center frequency were obtained, providing a fractional tuning range comparable to a dye laser. Bridgman-grown crystals were cleaved into parallelepipeds with cavity lengths from  $0.1$  to  $1 \text{ mm}$ . A Q-switched Nd:YAG laser operating at  $1.06 \mu\text{m}$  in a  $\text{TEM}_{00}$  mode was used as the excitation source and focused into a line image across the length of the sample. Both annealed and as-grown samples having electron concentrations ranging from  $2 \times 10^{17}$  to  $6 \times 10^{18} \text{ cm}^{-3}$  were made to lase near liquid helium temperature. The measured spontaneous linewidths were consistent with calculated values based on reasonable values for the electron effective mass. In a single alloy composition near liquid helium temperature, laser action occurred in a number of modes in a spectral range up to 10 percent of the center frequency. The spacing of longitudinal modes for a given spatial mode ranged from  $8$  to  $< 1 \text{ cm}^{-1}$  for the range of cavity lengths used, and occurred over nearly the entire spontaneous bandwidth for a given sample. A study of the time-resolved spectra indicated that lasing tended to occur in all modes simultaneously with no evidence of mode switching.

## Section II



The present laser emission bandwidths are an order-of-magnitude greater than those reported for electron-beam-pumped<sup>11</sup> lead salt lasers, and nearly two-orders-of-magnitude greater than those reported for lead salt diode<sup>12</sup> lasers in the infrared. Fine tuning of the modes by changing the crystal temperature<sup>13</sup> resulted in nearly continuous coverage over the entire spontaneous bandwidth for each alloy composition.

A. Mooradian  
A. J. Strauss  
J. A. Rossi

### C. HIGH-RESOLUTION SPECTROSCOPY OF ATMOSPHERIC WATER VAPOR

Three absorption lines of atmospheric water vapor in the  $\nu_2$ -band near  $5.32 \mu\text{m}$  have been fully resolved using a CW tunable  $\text{PbS}_{0.6}\text{Se}_{0.4}$  semiconductor laser. These data represent the first high-resolution study providing complete resolution ( $= 3 \times 10^{-5} \text{ cm}^{-1}$ ) of atmospheric water vapor in the infrared. They reveal significant discrepancies between the calculated and measured linewidths.<sup>14-16</sup> The laser used in these experiments was mounted on the cold finger of a liquid helium dewar at a temperature of about  $15^\circ\text{K}$ . Frequency-tuning was accomplished by varying the diode current with a measured tuning rate of  $572 \text{ MHz/mA}$ . In these experiments, the laser radiation was transmitted across a  $7.4\text{-m}$  path in the laboratory with a measured humidity of 18 percent and a temperature of  $22^\circ\text{C}$ . The corresponding partial pressure of water vapor is 3.6 torr giving a concentration of  $\sim 3.8 \times 10^{-6} \text{ g/cc}$  of water vapor in the air. Figure II-4 shows the laser transmission through the  $7.4\text{-m}$  path as a function of frequency. Three strong absorption lines labeled A, B, and C are observed and readily identified as members of the  $\nu_2$  fundamental vibration band using a grating spectrometer and published water-vapor line positions.<sup>16</sup> Since the laser output power is not a strong function of current, it is relatively easy to estimate the output power at the absorption lines (dashed line) and, hence, to deduce the absorption profile of these lines. Table II-2 summarizes the measured relative positions, linewidths, and intensities for the three lines. In this table, we list the positions of the two weaker lines relative to the strong center line since our laser calibration is not absolute, i.e., only the tuning rate has been measured.

The experimental intensities were obtained by first reducing the absorption data  $\propto e^{-\alpha L}$  to obtain the absorption coefficient as a function of frequency  $\alpha(f)$ . This function was then integrated graphically. The absorption constant obtained from the data of Fig. II-4 is probably not accurate in the wings  $>1$  to  $2 \text{ GHz}$  from the line center due to difficulties in estimating the background. However, the main contributions to the absorption for these lines are within  $\pm 1$  to  $2 \text{ GHz}$  and the measured intensities should be accurate. Figure II-5 shows the absorption coefficient deduced from the strong central line of Fig. II-4, line B, and known to be at  $1879.34 \text{ cm}^{-1}$ . The Lorentzian lineshape shown is adjusted to provide the same peak absorption and linewidth as the measured curve. The Doppler width of water vapor at this temperature is  $165 \text{ MHz}$  or about  $1/6$  of the measured width of this line.

There is considerable discrepancy between the measured and calculated values of the linewidths and relative positions as given in Table II-2. All three lines are much narrower than expected. While these transitions involving high  $J$  ( $>10$ ) are expected to have relatively small  $\text{N}_2$  and  $\text{O}_2$  collision broadening, the measured width of line A is only about 25 percent of the calculated width. It is surprising that line A has a full width which is only three times the



TABLE II-2  
WATER VAPOR ABSORPTION IN THE  $\nu_2$ -BAND (010-000)

Line	Rotational Transition	Frequency ( $\text{cm}^{-1}$ )	$\Delta F(\text{cm}^{-1})$		Halfwidth <sup>†</sup> ( $\text{cm}^{-1}$ )		Intensity ( $\text{cm}^{-1}/\text{g cm}^{-2}$ )	
		Ref. 3	Measured	Ref. 3	Measured	Ref. 3	Measured	Ref. 3
A	16(1,16) $\leftarrow$ 15(0,15)	1879.01	-0.29	-0.33	0.0084	0.032	1.98	1.58
B	13(1,12) $\leftarrow$ 12(2,11)	1879.34	0*	0*	0.0174	0.034	12.30	12.12
C	13(2,12) $\leftarrow$ 12(1,11)	1879.60	0.32	0.26	0.0157	0.034	3.32	4.04

\* Assumed zero for reference.  
† Halfwidth at half absorption coefficient.

limiting low-pressure Doppler width of 165 MHz. The relative position discrepancies for lines A and C are  $0.04$  and  $0.06 \text{ cm}^{-1}$ , respectively. Note that these position inaccuracies are more than three times the measured linewidths.

To summarize, agreement between the measured and calculated line intensities for all three lines is quite good. The significant discrepancies are in the measured linewidths and relative line positions. The inaccuracies in the calculated linewidths yield calculated absorption coefficients which are two to four times smaller than those measured. Our results demonstrate the usefulness of tunable lasers for atmospheric propagation studies. They also indicate that theoretical models for calculating collision broadening and line positions are inadequate for the prediction of atmospheric water-vapor absorption for high J lines such as those studied here.

K. W. Nill      A. R. Calawa  
F. A. Blum    T. C. Harman  
P. L. Kelley

#### D. DETERMINATION OF TOTAL BAND INTENSITY AND TRANSITION MOMENT FOR THE $\nu_1$ -BAND OF $\text{SO}_2$

We continue our analysis<sup>17</sup> of the  $\nu_1$ -band of  $\text{SO}_2$  using data obtained with PbSnTe diode lasers. The strengths of several rather isolated  $\text{SO}_2$  lines were determined from their peak absorption constants and linewidths at a pressure of 10 torr. Table II-3 gives the transitions, their measured intensities, and the projected values for total band intensity obtained by dividing the measured intensity for each line by its calculated fractional contribution to the band. Figure II-6 is a plot of measured line intensity vs the calculated fractional contribution. From the data, we find an average of the total intensity of the  $\nu_1$ -band of  $358 \pm 20 \times 10^{-20} \text{ cm}^{-1} \text{ mol}^{-1} \text{ cm}^2$  (the slope of the solid line in the figure). This value is consistent with the value  $371 \pm 20 \times 10^{-20} \text{ cm}^{-1} \text{ mol}^{-1} \text{ cm}^2$  found by Burch, *et al.*,<sup>18</sup> and within the range quoted by earlier workers,<sup>19-21</sup> employing the integrated-band technique. By using our value of band strength, an effective vibrational transition moment of  $|\mu_{ij}| = 0.086 \pm 0.003 \text{ D}$  is found.

E. D. Hinkley    A. R. Calawa  
S. A. Clough<sup>†</sup>   P. L. Kelley

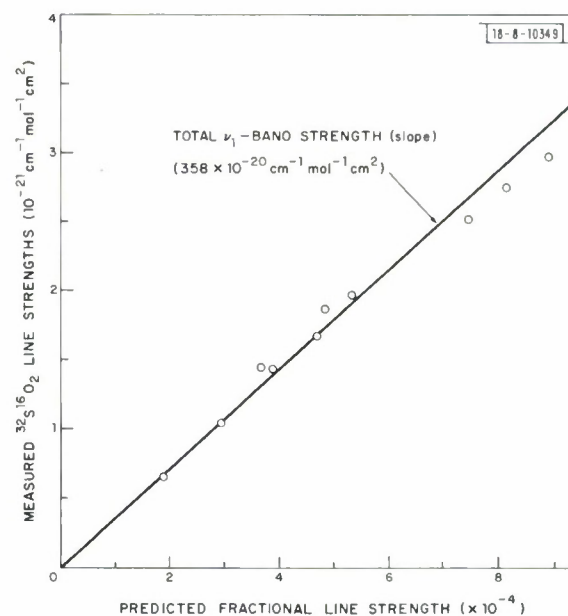
<sup>†</sup>Optical Physics Laboratory, Air Force Cambridge Research Laboratories.



Transition* $J'_{K'_A, K'_C} \leftarrow J''_{K''_A, K''_C}$	Frequency ( $\text{cm}^{-1}$ )	Measured Intensity ( $\text{cm}^{-1} \text{mol}^{-1} \text{cm}^2$ )	Projected Total Band Intensity ( $\text{cm}^{-1} \text{mol}^{-1} \text{cm}^2$ )
$30_{10,20} \leftarrow 30_{11,19}$	1115.031	$0.66 \times 10^{-21}$	$351 \times 10^{-20}$
$23_{5,19} \leftarrow 24_{6,18}$	1116.962	1.44	392
$18_{6,12} \leftarrow 19_{7,13}$	1117.038	1.67	356
$13_{7,7} \leftarrow 14_{8,6}$	1117.128	1.96	367
$22_{9,13} \leftarrow 22_{10,12}$	1118.956	1.04	354
$8_{0,8} \leftarrow 8_{1,7}$	1148.810	2.96	332
$6_{0,6} \leftarrow 6_{1,5}$	1149.346	2.74	336
$2_{1,1} \leftarrow 2_{0,2}$	1153.488	1.43	368
$5_{1,5} \leftarrow 4_{0,4}$	1156.195	1.86	384
$14_{1,13} \leftarrow 14_{0,14}$	1156.842	2.51	336

\* Conventional spectroscopic notation is followed, where the upper state is listed first.

Fig. II-6. Measured line strength vs calculated fractional line strength.



## REFERENCES

1. J. A. Rossi, S. R. Chinn and A. Mooradian, Appl. Phys. Letters 20, 84 (1972).
2. P. D. Dapkus, N. Holonyak, Jr., J. A. Rossi, D. A. High and F. V. Williams, J. Appl. Phys. 40, 3300 (1969).
3. W. M. Coderre and J. C. Wooley, Can. J. Phys. 48, 463 (1969).
4. D. T. F. Marple, J. Appl. Phys. 35, 1241 (1964).
5. T. E. Zachos, IEEE J. Quantum Electron. QE-5, 29 (1969).
6. I. Melngailis and R. H. Rediker, J. Appl. Phys. 37, 899 (1966), DDC AD-642173.
7. U. Heim, O. Röder and M. H. Pilkuhn, Solid State Commun. 7, 1173 (1969).
8. T. L. Paoli, J. E. Ripper and T. H. Zachos, IEEE J. Quantum Electron. QE-5, 271 (1969).
9. P. P. Sorokin, J. D. Lax and J. R. Lankard, J. Appl. Phys. 34, 2553 (1963).
10. J. R. Packard, W. C. Tait and D. A. Campbell, IEEE J. Quantum Electron. QE-5, 44 (1969).
11. C. E. Hurwitz, A. R. Calawa and R. H. Rediker, IEEE J. Quantum Electron. QE-1, 102 (1965), DDC AD-622308.
12. J. F. Butler, A. R. Calawa, R. J. Phelan, Jr., A. J. Strauss and R. H. Rediker, Solid State Commun. 2, 303 (1964), DDC AD-453105; J. F. Butler and A. R. Calawa, J. Electrochem. Soc. 112, 1056 (1965), DDC AD-623624.
13. E. D. Hinkley, T. C. Harman and C. Freed, Appl. Phys. Letters 13, 49 (1968), DDC AD-677847.
14. W. S. Benedict and L. D. Kaplan, J. Chem. Phys. 30, 388 (1959).
15. ———, J. Quant. Spectr. Radiative Transfer 4, 453 (1964).
16. W. S. Benedict and R. F. Calfee, Line Parameters for the 1.9 and 6.3 Micron Water Vapor Bands (Government Printing Office, Washington, D. C., 1967).
17. Solid State Research Report, Lincoln Laboratory, M. I. T. (1971:4), p. 25, DDC AD-736501.
18. D. E. Burch, J. D. Pembroke and D. A. Gryvnak, private communication.
19. J. Morcillo and J. Herranz, Anales Real Soc. Espan. Fis. Quim. (Madrid) A 52, 207 (1956).
20. J. E. Mayhood, Can. J. Phys. 35, 954 (1957).
21. D. F. Eggers, Jr. and E. D. Schmid, J. Phys. Chem. 64, 279 (1960).

### III. MATERIALS RESEARCH

#### A. ENERGY BANDS IN $\text{TX}_2$ COMPOUNDS WITH PYRITE, MARCASITE, AND ARSENOPYRITE STRUCTURES

Hulliger and Mooser<sup>1</sup> correlated the number of transition-metal, or T-ion, d electrons with crystal structure in the compounds  $\text{TX}_2$ ,  $\text{TX}_2\text{Y}$ , and  $\text{TY}_2$  having the pyrite, marcasite, or arsenopyrite structures. All three structures are characterized by diatomic anions: formally  $(\text{X}_2)^{2-}$ ,  $(\text{XY})^{3-}$ , and  $(\text{Y}_2)^{4-}$ , where X is a chalcogen and Y is a pnigogen. The number of d electrons per cation is then obtained from the formal valence of the cation. Thus,  $\text{FeS}_2$  has a d-state manifold per iron atom  $d^6$ ,  $\text{FeSAs}$  has  $d^5$ , and  $\text{FeAs}_2$  has  $d^4$ . Empirically, where the  $d^n$  manifold has  $n = 0, 2$ , or  $4$ , the marcasite structure is formed; where  $n = 5$ , either a high-spin  ${}^6A_1(d^5)$  configuration in the pyrite structure or a low-spin configuration in the arsenopyrite structure is formed; and where  $n \geq 6$ , the pyrite structure is generally found, although a marcasite phase with anomalously large axial ratios may also occur. A few compounds, including  $\text{FeS}_2$ , exhibit both the anomalous marcasite and pyrite phases.

In all three structures, each cation occupies a distorted octahedral site. The cubic pyrite structure, which is shown in Fig. III-1(a-c), contains corner-shared octahedra, and the crystal field at each T-ion has trigonal symmetry. In the orthorhombic marcasite structure of

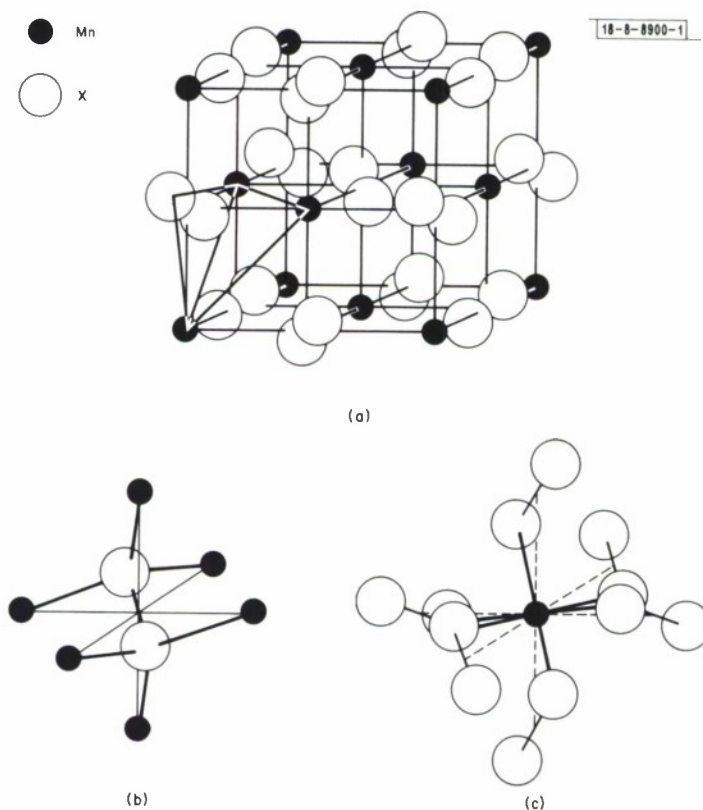


Fig. III-1(a-c). The pyrite structure.

### Section III

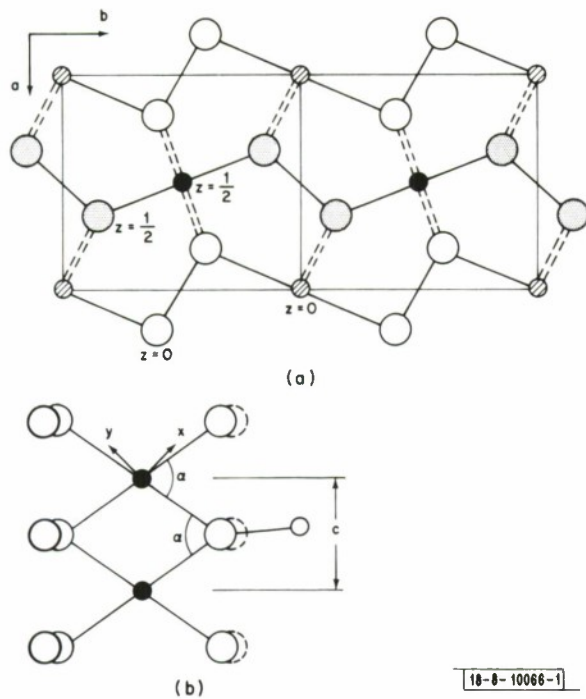


Fig. III-2. The orthorhombic marcasite structure; (a) projection onto a-b plane, (b) c-axis chain in regular marcasite structure.

Fig. III-3. Hulliger-Mauser one-electron d-level scheme per cation; free atom (a), and octahedral-site splittings in (b) cubic, (c) pyrite, (d) marcasite and (e) arsenopyrite crystalline fields.

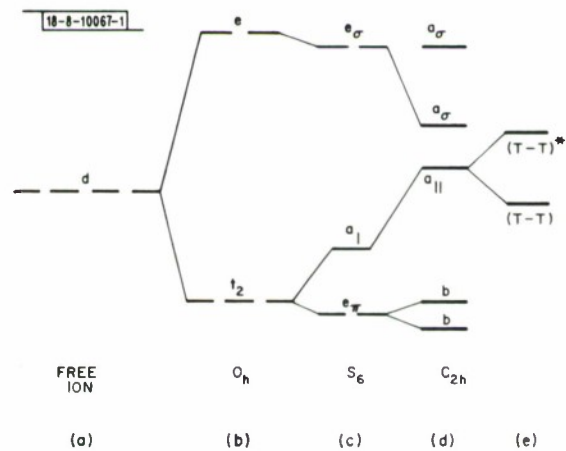


Fig. III-2(a-b), on the other hand, linear chains of edge-shared octahedra run parallel to the orthorhombic c-axis. Regular marcasite has a cation-anion-cation angle  $\alpha < 90^\circ$ , and anomalous marcasite has  $\alpha > 90^\circ$ . Finally, the monoclinic arsenopyrite structure is a distorted marcasite in which chains of cations parallel to the c-axis form alternately short and long separations.

Hulliger and Mooser<sup>1</sup> pointed out that the one-electron d-orbitals would be split by the crystalline fields as indicated in Fig. III-3(a-e). With the assumption that these splittings are large compared with any bandwidths, they showed that the structural, magnetic, and electrical properties could be qualitatively harmonized. However, there are several serious defects to such a localized-electron model, including the postulate that the arsenopyrite structure is due to T-T homopolar bonding along the c-axis. Brostigen and Kjekshus<sup>2</sup> subsequently argued that the arsenopyrite structure represents an expansion, not a contraction, of alternate metal-metal separations along the c-axis, but they made the mistake of attributing this to T-T interactions. Previous discussions of this problem fail to consider adequately the role of covalent mixing between the cation-d and anion-p orbitals.

From general physical considerations, it is possible to show that there is a transition from localized to itinerant character of the outer d electrons as the ratio  $W/U$  increases through unity. From tight-binding theory, the bandwidth is

$$W \approx 2zb \quad (\text{III-1})$$

where  $z$  is the number of nearest neighbors, and  $b$  is the usual transfer-energy matrix element for d-electron transfer between like cations. In the compounds under consideration, the cation-anion-cation interactions dominate any cation-cation interactions, and  $b \sim \epsilon\lambda^2$ , where  $\epsilon$  is a one-electron energy and  $\lambda$  is the covalent-mixing parameter for cation-d and anion-p interactions. The energy

$$U = E_{n+1} - E_n \quad (\text{III-2})$$

is the difference between the ground-state energies for the  $d^{n+1}$  and the  $d^n$  manifolds. Since  $U$  decreases with increasing radial extension of the crystal-field wave functions, the ratio  $W/U$  increases unambiguously with increasing  $\lambda$ . Therefore, it is possible to predict qualitatively whether a given compound will have localized d-electrons because  $W/U \ll 1$ , or itinerant d-electrons because  $W/U \gg 1$  by making comparisons with other compounds whose physical properties are known. From the physical properties of several transition-metal sulfides and selenides, there appears to be a transition from localized  $\sigma$ -bonding d-electrons at  $\text{Mn}^{2+}$  ions to itinerant  $\sigma$ -bonding d-electrons at  $\text{Ni}^{2+}$  ions.

Figures III-4 and III-5 represent the schematic energy-level diagrams for  $\text{MnS}_2$  and  $\text{FeS}_2$  having the pyrite structure. In  $\text{MnS}_2$ , the localized-electron ground-state manifold  ${}^6A_1(d^5)$  is shown as a discrete many-electron energy  $E_5$ . Actually, magnetic interactions will broaden this level by at least the width of the spin-wave spectrum. The semiconductor  $\text{FeS}_2$  is known to contain  $\text{Fe}^{2+}$  ions in the low-spin state, which indicates that the d-electrons should be described by a one-electron band (itinerant-electron) model. Ferromagnetic, metallic  $\text{CoS}_2$  contains one  $\sigma$ -bonding d-electron in a strongly correlated band, which shows that the  $\sigma^*$  bands are narrow ( $W/U \lesssim 1$ ).  $\text{NiS}_2$  and  $\text{NiSe}_2$  each have a half-filled  $\sigma^*$  band. In antiferromagnetic  $\text{NiS}_2$ , but not in metallic  $\text{NiSe}_2$ , this band is just split in two by the electron correlations ( $W/U \approx 1$ ).



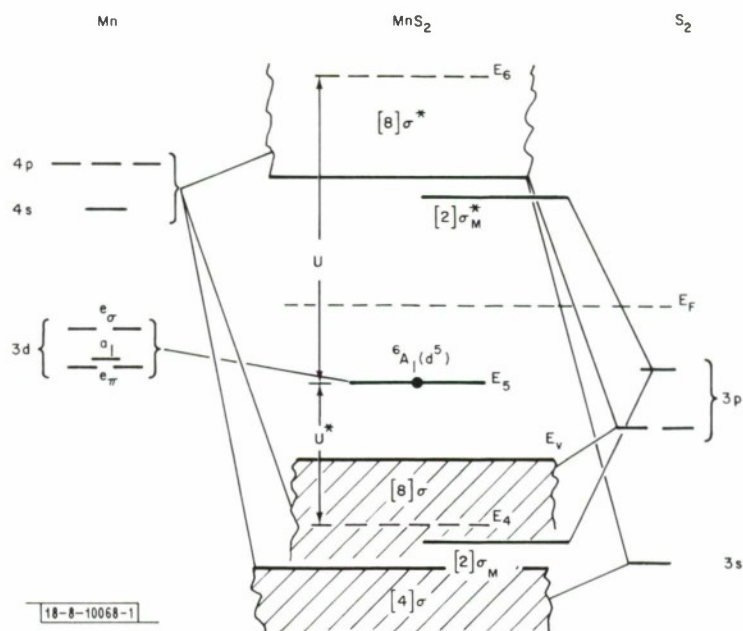


Fig. III-4. Energy-level scheme for  $\text{MnS}_2$ . One-electron energies for s- and p-bands, energy  $E_5$  of  ${}^6A_1(d^5)$  single-atom manifolds and energies  $E_6$  and  $E_4$  of  $d^6$  and  $d^4$  single-atom manifolds. Numbers in brackets refer to states per molecule.

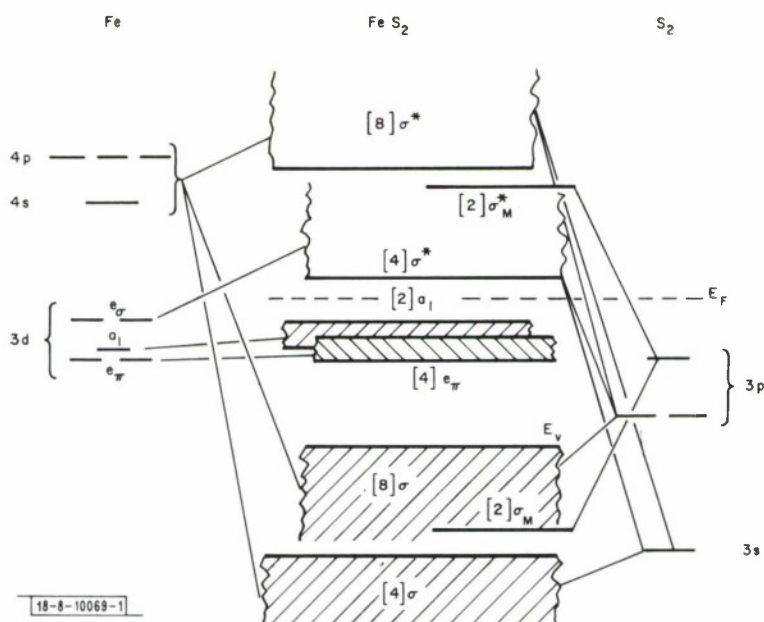


Fig. III-5. Energy bands for  $\text{FeS}_2$  with pyrite structure.

Metallic  $\text{CuS}_2$ , which becomes superconducting at lowest temperatures, has no spontaneous magnetization. This is consistent with an increasing  $\lambda$  on going to heavier cations, and from sulfur to selenium.

The essential difference between the band structures of the pyrites and the marcasites or arsenopyrites is the splitting of the  $t_{2g}$ -orbitals, as shown in Fig. III-3(c-e). From geometrical considerations, the  $a_{||}$ -orbital directed along the c-axis is not orthogonal to the  $\sigma$ -bonding anion orbitals, whereas the two b-orbitals are nearly so. Therefore, the  $a_{||}$ -orbital is distinguished from the two b-orbitals by relatively strong covalent mixing with the anion orbitals, and the strength of this mixing increases with the deviation of  $\alpha$  from  $109^\circ$ , where  $\alpha$  is defined by Fig. III-2(b). Since the d-orbitals are antibonding with respect to the anion array, covalent mixing raises the  $a_{||}$ -orbital above the two b-orbitals as shown in Fig. III-3(d). The fact that  $\text{FeAs}_2$  is a diamagnetic semiconductor requires that in  $\text{FeAs}_2$  the covalent mixing is strong enough to create itinerant d electrons and to raise the  $a_{||}$ -band completely above any narrow b-bands, as shown in Fig. III-6.

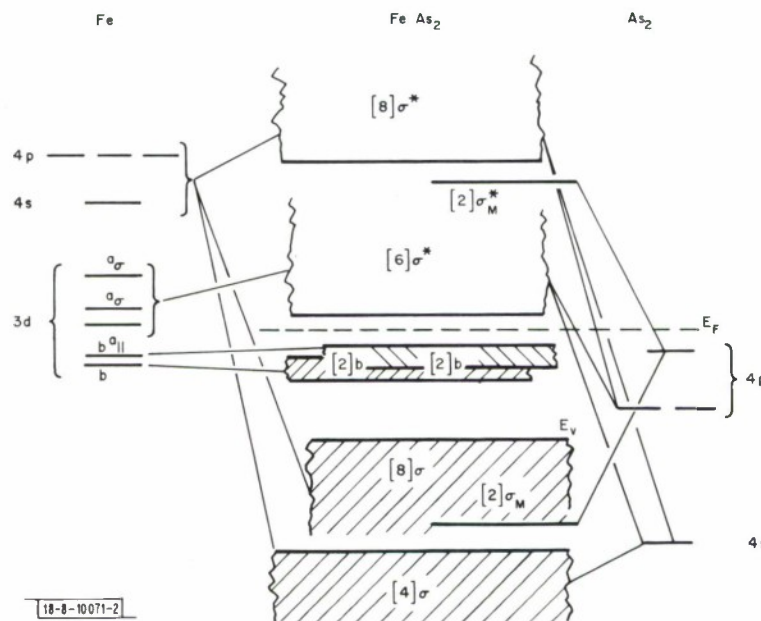


Fig. III-6. Energy bands for  $\text{FeAs}_2$  with regular marcasite structure.

Since covalent mixing stabilizes anion p-orbitals at the expense of cation d-orbitals, stronger covalent mixing occurs with empty d-orbitals. The marcasite structure allows  $\sigma$ -bond covalent mixing with the two  $a_\sigma$ - and the  $a_{||}$ -orbitals, bonding with the  $a_{||}$ -orbital being larger the smaller the angle  $\alpha$ . Therefore, regular marcasite should be the competitive  $\text{TX}_2$  structure for T cations having a localized  $d^2$  or  $d^7$  configuration (antiferromagnetic  $\text{CrSb}_2$  has  $d^2$ ), or a nonmagnetic  $d^4$  configuration as in  $\text{FeAs}_2$ ; and the relatively small axial ratios  $c/a$  and  $c/b$  in the regular marcasite structure are due to cation-anion bonding, not to cation-cation bonding. For a nonmagnetic  $d^6$  configuration, the  $a_{||}$ -bands would be occupied. This must reduce the stability of covalent mixing and hence decrease the angle  $\alpha$  to produce an anomalous marcasite structure. With a more stable, narrower  $a_{||}$ -band, the band structure would be similar to that

### Section III

for the pyrite structure. Therefore, these two structures become competitive with each other, which is in accord with the appearance of the two polymorphs of  $\text{FeS}_2$ .

The fact that the arsenopyrite structure is uniquely associated with compounds having a non-magnetic  $d^5$  configuration also follows from these considerations. Given the band scheme of Fig. III-6 for a  $d^4$  configuration, a nonmagnetic  $d^5$  configuration would have a half-filled  $a_{||}$ -band if it crystallized in the marcasite structure. However, a narrow, half-filled band may induce a crystallographic distortion that changes the structural periodicity so as to split the band in two, thereby stabilizing occupied states at the expense of unoccupied states. Since the  $a_{||}$ -orbitals are directed along the c-axis, a doubling of the periodicity along the c-axis by increasing  $\alpha$  for alternate metal-metal separations would stabilize the occupied states in the  $a_{||}$ -band. This is

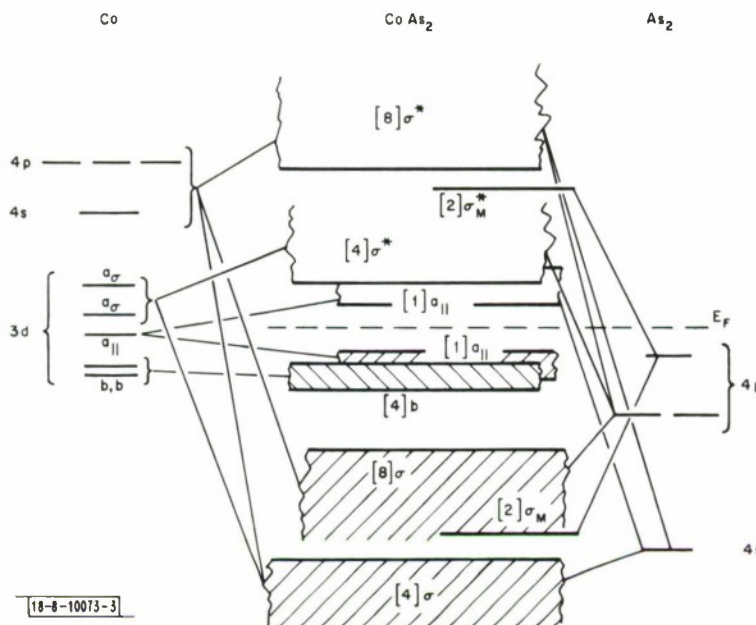


Fig. III-7. Energy bands for  $\text{CoAs}_2$  with arsenopyrite structure.

the distortion found in the arsenopyrite structure of  $\text{CoAs}_2$ , for example. Significantly, the model predicts a larger d-electron density within the larger separations than within the smaller ones, since the deformations are not due to metal-metal bonding, but to metal-anion bonding. The band structure for  $\text{CoAs}_2$  is shown in Fig. III-7. It is to be contrasted with that for  $\text{MnS}_2$  in Fig. III-4, which represents an antiferromagnet with high-spin  $d^5$  configuration. Clearly a  $\text{Co}^{4+}$  ion would have much stronger covalent bonding with arsenic than an  $\text{Mn}^{2+}$  ion has with sulfur.

J. B. Goodenough

#### B. EFFECT OF CARRIER GAS VELOCITY ON SUPERSATURATION REQUIRED FOR VAPOR PHASE CRYSTAL GROWTH

The pressure  $p_0$  of the vapor in equilibrium with a solid decreases with decreasing temperature  $T$  according to the expression

$$p_0 = A \exp[-\Delta H/RT] \quad (\text{III-3})$$

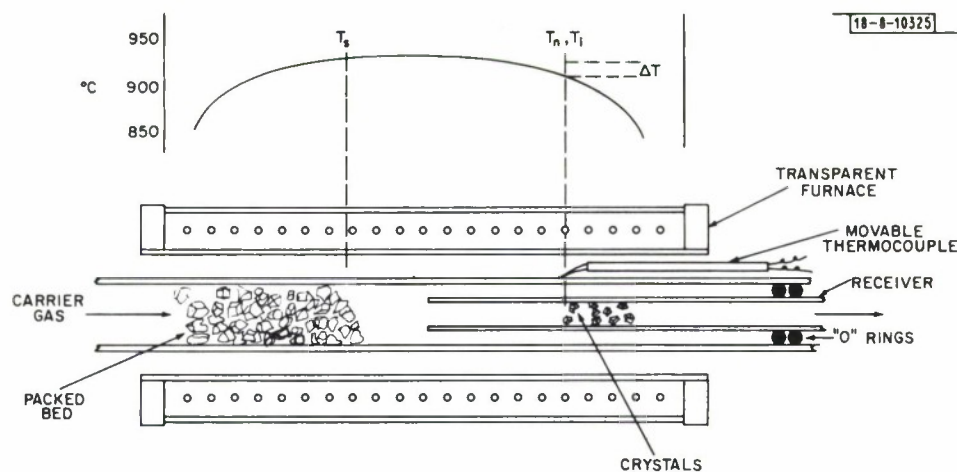


Fig. III-8. Schematic diagram of apparatus for open-tube growth of single crystals from vapor phase.

where  $\Delta H$  is the heat of vaporization and  $R$  is the gas constant. One of the standard methods for utilizing this property in the growth of single crystals from the vapor phase is the open-tube technique represented schematically in Fig. III-8. A carrier gas passes through a charge bed of polycrystalline source material at temperature  $T_s$ , becomes saturated with vapor at this temperature, and transports the vapor downstream to a receiver tube where the solid is deposited in single-crystal form. In general, deposition does not take place at  $T_s$ , as it would if crystal growth were an equilibrium process, but begins at a lower temperature  $T_i$ , where the vapor is said to be supersaturated because the equilibrium vapor pressure  $p_o$  is less than the actual vapor pressure  $p$ . The degree of saturation  $\sigma$  is defined as the ratio  $p/p_o$ . Since, in this case,  $p$  is equal to the equilibrium vapor pressure at  $T_s$ , according to Eq. (III-3) the degree of saturation at  $T_i$  can be found from

$$\sigma = \exp \left[ \frac{\Delta H(1/T_i - 1/T_s)}{R} \right] \quad (\text{III-4})$$

even though it would not be feasible to measure  $p$  at the crystal-gas interface directly.

In studies on the open-tube vapor growth of various materials, including As,  $\text{Cd}_3\text{As}_2$ , CdTe, and ZnTe, and also on the epitaxial growth of GaAs and InAs by halogen transport, we made a number of qualitative observations indicating that the degree of saturation required for crystal growth is strongly affected by the velocity of the carrier gas. For growth in tubes of uniform diameter, at both low and high flow rates  $T_i$  could be as much as  $100^\circ\text{C}$  below  $T_s$ , but at intermediate rates it was occasionally within a few degrees of  $T_s$ . In tubes containing constrictions, crystals frequently grew only in regions of intermediate diameter, where the gas velocity had intermediate values; the same observation has been made by Vohl<sup>3</sup> and Iseler.<sup>4</sup> Finally, crystals never grew laterally to the point where they completely blocked the growth tube and stopped the gas flow.

On the basis of these observations, we made a series of experiments on the vapor growth of ZnTe in order to determine quantitatively the manner in which the degree of saturation required for growth depends on the carrier gas velocity. The experimental apparatus (Fig. III-8) was



### Section III

made of fused silica and heated by means of a transparent furnace, so that the formation and vaporization of crystals could be observed in situ. Receiver tubes of four different diameters were used to observe crystal growth at four different gas velocities for each rate of gas flow through the charge bed of polycrystalline ZnTe. The temperature at any point in the system could be measured by movable thermocouples.

In a typical experiment, the carrier gas ( $H_2$ ) was passed slowly through the growth apparatus while the system was heated to establish a temperature profile such as that shown in Fig. III-8. The rate of gas flow was then increased, resulting in the nucleation and growth of crystals in the receiver. When no further nucleation occurred, the temperature of the hottest crystal was measured to determine the nucleation temperature  $T_n$ . The receiver was then moved a short distance toward the charge bed, increasing its temperature and causing some of the crystals to evaporate. When no further evaporation occurred, the temperature of the hottest crystal remaining was taken as  $T_i$ . The temperature at the end of the charge bed nearest the receiver, which was the highest temperature along the bed, was taken as  $T_s$ . To obtain additional experimental points, the growth conditions were changed and the values of flow rate,  $T_i$ , and  $T_s$  were measured again.

The results obtained by this procedure for the four receivers are shown in Fig. III-9, where the differences,  $\Delta T = T_s - T_i$ , are plotted against the measured  $H_2$  flow rate. [The ordinate scale in Fig. III-9 gives values of  $\sigma$  calculated according to Eq. (III-4), as well as  $\Delta T$  values.] Data are consistent with the qualitative observations described above, since  $\Delta T$  is between  $10^\circ$  and  $30^\circ C$  at the lowest flow rates and with increasing flow rate decreases to a minimum close to zero, after which it increases significantly. With increasing receiver diameter, the minimum

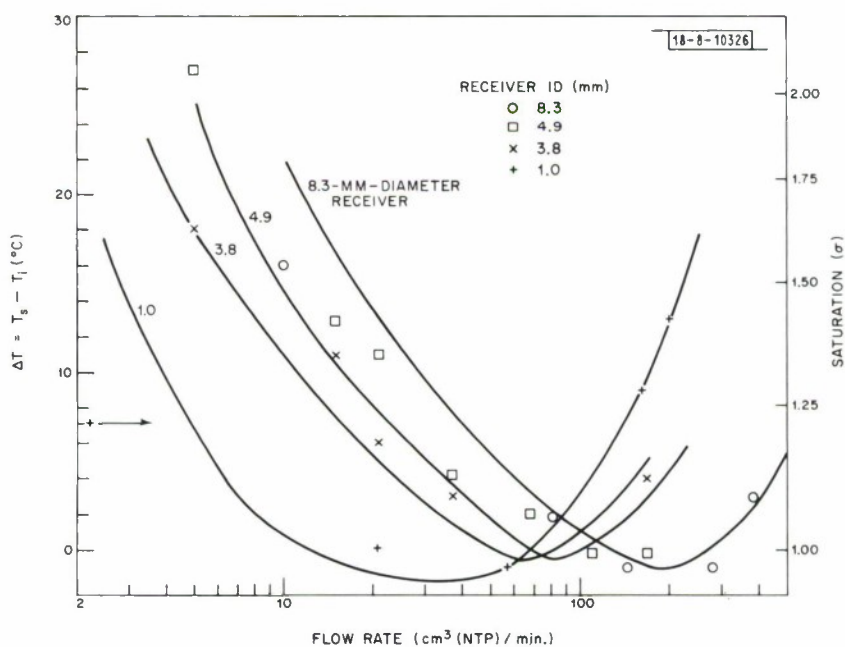


Fig. III-9. Difference between saturation temperature and interface temperature,  $\Delta T = T_s - T_i$ , as a function of carrier gas flow rate in vapor growth of ZnTe.



is displaced to higher flow rate. If  $\Delta T$  is plotted against carrier gas velocity, which is proportional to the flow rate divided by the square of the receiver diameter, separate curves are still obtained for the four receivers. In this case, the position of the  $\Delta T$  minimum shifts to lower velocity with increasing receiver diameter.

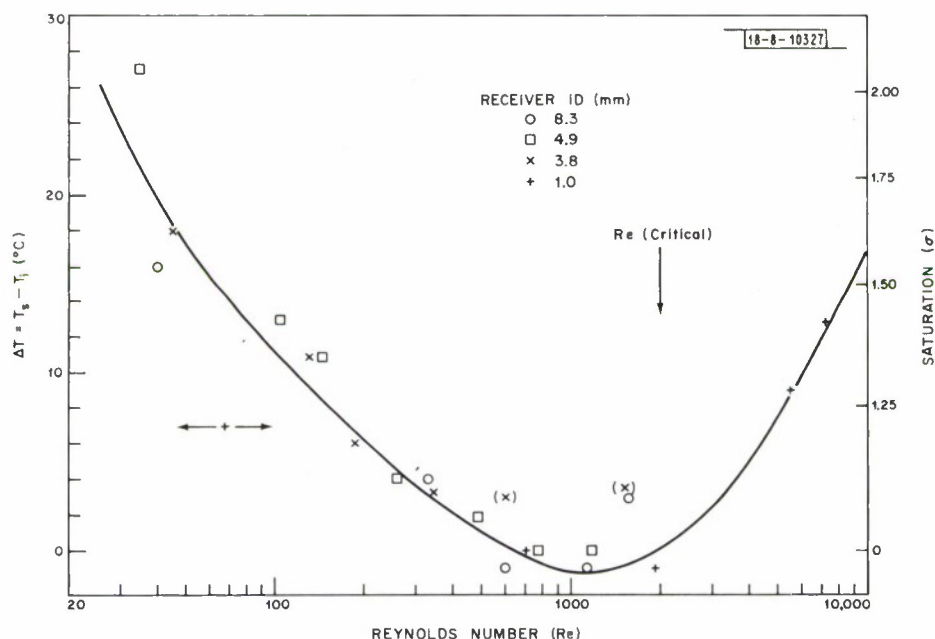


Fig. III-10. Variation of  $\Delta T = T_s - T_i$  with Reynolds number in vapor growth of ZnTe.

In Fig. III-10, the measured values of  $\Delta T$  are plotted against the Reynolds number, defined as  $Re \equiv vdp/\mu$ , where  $v$  is the velocity of a gas of density  $\rho$  and viscosity  $\mu$  flowing in a tube of diameter  $d$ . Data for all four receivers now fall on a single curve. The minimum in  $\Delta T$  occurs at  $Re$  of 1000 to 2000, close to the boundary between laminar flow (which occurs for  $Re$  less than  $\sim 2000$ ) and turbulent flow (which occurs for greater  $Re$  values).

T. B. Reed  
W. J. LaFleur

### C. IMPURITY PROFILES OF EVAPORATED GOLD FILMS DETERMINED BY AUGER ELECTRON SPECTROSCOPY

Gold films about  $200 \text{ \AA}$  thick are quite transparent in the visible region of the spectrum, but in the infrared they still exhibit the extremely high-reflectivity characteristic of bulk gold. We have found<sup>5</sup> that transparent furnaces operating to about  $1100^\circ\text{C}$  in air can be constructed by using such films, deposited on the inside surface of Pyrex cylinders, to provide reflective thermal insulation. To obtain satisfactory adherence of the gold, the Pyrex cylinder is first coated with a very thin layer (about  $50 \text{ \AA}$ ) of nichrome (75% Ni, 12% Fe, 11% Cr, 2% Mn) or Kanthal (72% Fe, 22% Cr, 5.5% Al) by vacuum evaporation from an alloy wire placed at the axis of the cylinder. Without breaking the vacuum, the gold is immediately deposited by evaporation of a gold layer electroplated on a similarly placed 0.75-mm-diameter tungsten wire.

### Section III

Still better adherence is obtained by annealing the composites at 600°C in air for 16 hours. In order to determine the effect of annealing on the distribution of the elements in the films, we have had test samples analyzed by Auger electron spectroscopy.<sup>†</sup> Since the penetration depth for this technique is only about 10 Å, a composition profile can be obtained by performing an analysis, removing a few atomic layers from the sample surface by ion sputtering, performing a second analysis, etc.

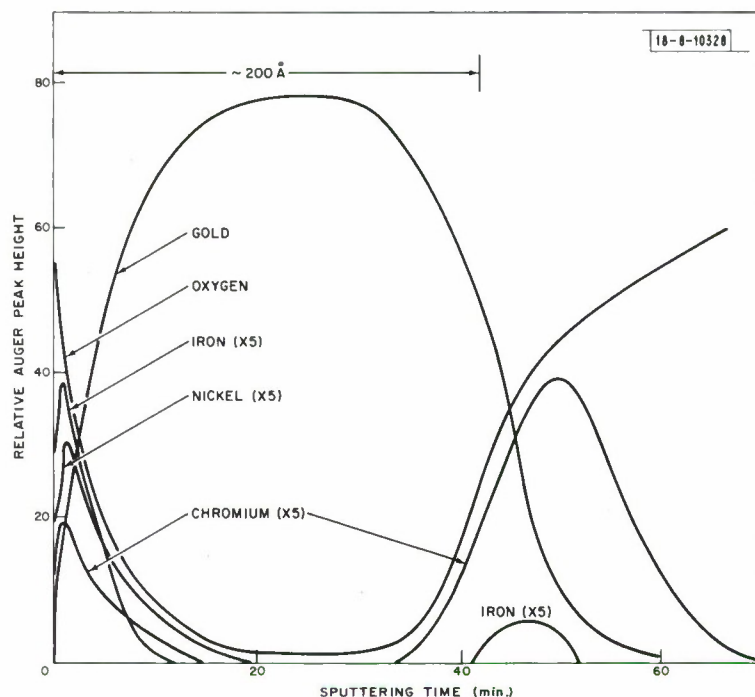


Fig. III-11. Distribution of elements in annealed gold-nichrome-Pyrex composite analyzed by Auger electron spectroscopy.

The Auger results for an annealed gold-nichrome-Pyrex composite are shown in Fig. III-11. Most of the Cr from the nichrome layer has remained in its original location adjacent to the Pyrex, while the Ni and most of the Fe have migrated to the outer surface of the gold layer. We attribute the differences in behavior of these three elements to their differences in oxygen affinity, which increases in the order  $\text{Ni} < \text{Fe} < \text{Cr}$ , and to their low rates of diffusion through gold once they have been oxidized. According to this explanation, most of the Cr cannot diffuse through the gold layer because it is oxidized at the time of deposition or at the beginning of annealing, either by the Pyrex itself or by oxides (e.g., water) adsorbed on the Pyrex. Because of its low oxygen affinity, the Ni is not initially oxidized, and during annealing it diffuses to the outer surface of the gold, where it is oxidized by the air. The Fe, with intermediate oxygen affinity, exhibits intermediate diffusion behavior.

<sup>†</sup>Physical Electronics Corporation, Edina, Minnesota.

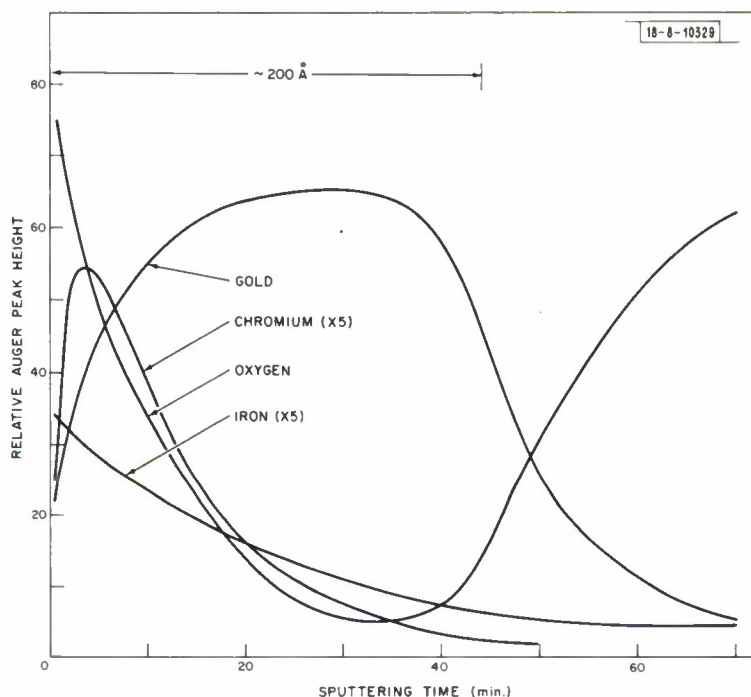


Fig. III-12. Distribution of elements in annealed gold-Kanthal-Pyrex compasite analyzed by Auger electron spectroscopy.

As shown in Fig. III-12, Auger analysis of an annealed gold-Kanthal-Pyrex composite shows that the Al migrates from the Kanthal layer to the outer surface of the gold. The Fe and Cr are mostly concentrated at this surface, but they are also found throughout the gold layer, and some Fe apparently diffuses into the Pyrex.

T. B. Reed  
W. J. LaFleur

#### D. Pb-RICH SOLIDUS OF $\text{PbS}_{0.63}\text{Se}_{0.37}$

Tunable diode lasers fabricated from  $\text{PbS}_{1-x}\text{Se}_x$  alloys can be used for ultrahigh-resolution infrared spectroscopy at shorter wavelengths than those accessible with  $\text{Pb}_{1-x}\text{Sn}_x\text{Te}$  alloys. Lasers made from  $\text{PbS}_{1-x}\text{Se}_x$  with  $0.35 \leq x \leq 0.40$  are of particular interest because they emit at wavelengths lying within an important absorption band of gaseous NO. We have determined the Pb-rich solidus between 300° and 850°C for alloys in this composition range.

All but two of the samples were cut from three large-grained ingots grown by the Bridgman method from nominally stoichiometric melts with an initial composition of  $x = 0.385$ . Electron microprobe analysis of several samples from these ingots gave compositions in the range  $0.35 \leq x \leq 0.39$ . The Se content of the other two samples may be somewhat lower, since they were obtained from an ingot whose initial melt composition was  $x = 0.358$ . This ingot and two of the other three contained numerous cracks, and samples cut from them cleaved very easily during handling, apparently because the ingots had been furnace-cooled too rapidly after growth. Samples from the remaining ingot, which was lowered slowly out of the furnace before the power was shut off, were considerably less fragile.

### Section III

As in undoped PbS and PbSe, the type and concentration of charge carriers in the  $\text{PbS}_{0.63}\text{Se}_{0.37}$  samples at room temperature and below are determined primarily by lattice defects associated with deviations from stoichiometry. All as-grown samples are n-type, with carrier concentrations of  $3$  to  $8 \times 10^{18} \text{ cm}^{-3}$  due to the presence of excess Pb. Thus, for alloys with  $x \approx 0.37$ , the solid phase in equilibrium with a stoichiometric melt is Pb-rich. In this respect, the alloys resemble PbS rather than PbSe, since the maximum melting composition of PbS is on the Pb-rich side of the stoichiometric composition, while the maximum melting composition of PbSe is on the Se-rich side.

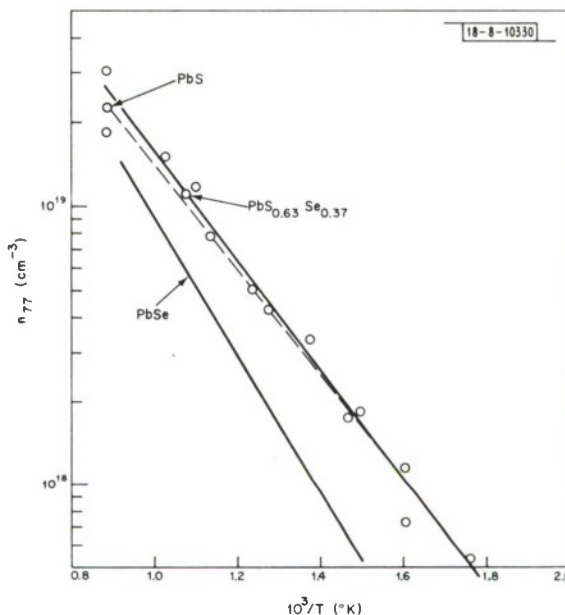
For both PbS and PbSe, the solubility of Pb along the Pb-rich solidus decreases with decreasing temperature, for temperatures up to at least  $850^\circ\text{C}$ . Because of this retrograde solubility, when a sample saturated with Pb at one temperature is cooled to a lower temperature, Pb tends to precipitate until the concentration of Pb remaining dissolved decreases to the solubility value for the lower temperature. Since the precipitated Pb is no longer electrically active, the carrier concentration decreases correspondingly. Therefore, the Pb-rich solidus curve can be determined by using Hall coefficient (R) measurements to determine the carrier concentrations (n) in samples that have been equilibrated by annealing and then quenched. Since the precipitation rate increases exponentially with temperature, the solidus determination can be made by this method up to the highest temperature from which samples can be quenched with sufficient speed to prevent precipitation during cooling, and down to the lowest temperature at which equilibrium can be reached by precipitation during the maximum time allowed for annealing.

We have used the same method to determine the Pb-rich solidus of  $\text{PbS}_{0.63}\text{Se}_{0.37}$  between  $300^\circ$  and  $850^\circ\text{C}$ . The samples were annealed in quartz ampoules which were sealed after being charged at room temperature with helium gas at a pressure of about 400 torr in order to increase the sample cooling rate during quenching. In most cases, a small quantity of  $\text{Pb}_{0.51}(\text{S}_{0.63}\text{Se}_{0.37})_{0.49}$  was also placed in the ampoule so that the sample could not become unsaturated by loss of Pb to the vapor phase. The annealing times ranged from 30 minutes at  $850^\circ\text{C}$  to 8 weeks at  $300^\circ\text{C}$ . No systematic study was made of the time required for equilibration as a function of annealing temperature, but in some cases annealing was repeated to make sure that equilibrium had been reached. Samples annealed at  $300^\circ$  and  $350^\circ\text{C}$  were air-quenched, while those annealed at higher temperatures were quenched by dropping the ampoules into water at room temperature.

The experimental data are shown in Fig. III-13, where the carrier concentration at  $77^\circ\text{K}$  ( $n = 1/R_{77}e$ ) is plotted on a logarithmic scale against the reciprocal absolute annealing temperature. As expected from the behavior of PbS and PbSe, the solubility of Pb in  $\text{PbS}_{0.63}\text{Se}_{0.37}$  is retrograde, with n decreasing from  $2.6 \times 10^{19} \text{ cm}^{-3}$  for  $850^\circ\text{C}$  to  $5.5 \times 10^{17} \text{ cm}^{-3}$  for  $300^\circ\text{C}$ . The values of n for the highest annealing temperatures are appreciably higher than those found for as-grown samples. The increase in n during annealing must have resulted from the dissolution of Pb precipitates that had been formed when the ingots were cooled after solidification, since the annealing times were too short for equilibrium to have been reached between the samples and the Pb-rich vapor phase supplied by  $\text{Pb}_{0.51}(\text{S}_{0.63}\text{Se}_{0.37})_{0.49}$ . Similar behavior is observed for PbS (see Ref. 6). The highest value of n measured for  $\text{PbS}_{0.63}\text{Se}_{0.37}$ ,  $2.6 \times 10^{19} \text{ cm}^{-3}$ , sets a lower limit on the concentration of excess Pb incorporated into the alloy when it is crystallized from a stoichiometric melt.



Fig. III-13. Pb-rich solidus lines of  $\text{PbS}_{0.63}\text{Se}_{0.37}$ ,  $\text{PbS}$  (Ref. 6), and  $\text{PbSe}$  (Ref. 7). Experimental points shown for  $\text{PbS}_{0.63}\text{Se}_{0.37}$  only.



The Pb-rich solidus data for  $\text{PbS}_{0.63}\text{Se}_{0.37}$  are well-represented by the straight line shown in Fig. III-13, which corresponds to the expression  $n = (1.44 \times 10^{21}) \exp[-(0.39 \text{ eV})/kT] \text{ cm}^{-3}$ . Solidus lines based on the published data for  $\text{PbS}$  (Ref. 6) and  $\text{PbSe}$  (Ref. 7) are also shown in Fig. III-13. It is somewhat surprising that the solidus for the alloy, which contains nearly 40 mole percent  $\text{PbSe}$ , is the same within experimental error as that for  $\text{PbS}$ , rather than intermediate between the lines for  $\text{PbS}$  and  $\text{PbSe}$ .

A. J. Strauss

#### REFERENCES

1. F. Hulliger and E. Mooser, *J. Phys. Chem. Solids* **26**, 429 (1965).
2. G. Brostigen and A. Kjekshus, *Acta Chem. Scand.* **24**, 2983 (1970).
3. P. Vohl, *Mater. Res. Bull.* **4**, 689 (1969).
4. G.W. Iseler, personal communication.
5. Solid State Research Report, Lincoln Laboratory, M.I.T. (1969:1), p. 21, DDC AD-690997.
6. A.J. Strauss, *Trans. Met. Soc. AIME* **239**, 794 (1967), DDC AD-661148.
7. R.F. Brebrick and E. Gubner, *J. Chem. Phys.* **32**, 170 (1962); A.R. Calawa, T.C. Harman, M. Finn and P. Youtz, *Trans. Met. Soc. AIME* **242**, 374 (1968), DDC AD-678986.



## IV. PHYSICS OF SOLIDS

### A. PHOSPHOR UPCONVERSION

#### 1. Rare-Earth Phosphors for Near-Infrared-to-Visible Upconversion

Investigation of conversion of near-infrared radiation to visible radiation by a gagarinite sample with nominal composition  $\text{NaY}_{0.81}\text{Yb}_{0.18}\text{Er}_{0.01}\text{F}_4$  has continued with a study of the excitation and emission spectra. In addition, measurements of the phosphor efficiency have been made, and primary efforts have concentrated on increasing the near-infrared input intensity in an attempt to establish the upper bounds of achievable efficiency.

The excitation spectrum, which is dependent upon the energy levels of the sensitizer (Yb), appears as a single peak with little structure, having a maximum near  $0.98\text{ }\mu\text{m}$  and a half-width of less than  $0.03\text{ }\mu\text{m}$ . This behavior differs significantly from the excitation spectra reported for the upconverting materials  $\text{LaF}_3\text{:Yb,Er}$ ,  $\text{GdF}_3\text{:Yb,Er}$ , and  $\text{YF}_3\text{:Yb,Er}$  (Ref. 1). The excitation spectra for these materials show considerable structure and are significantly broader, extending to shorter wavelengths. We have verified this with a sample of  $\text{Y}_{0.81}\text{Yb}_{0.18}\text{Er}_{0.01}\text{F}_3$ .<sup>†</sup> Although our sample had nearly double the upconversion at  $0.98\text{-}\mu\text{m}$  excitation, the  $\text{Y}_{0.81}\text{Yb}_{0.18}\text{Er}_{0.01}\text{F}_3$  sample showed greater visible emission for excitation wavelengths below  $0.95\text{ }\mu\text{m}$ . Thus, the relative efficiency of the two samples is strongly dependent upon the pump spectrum.

The emission spectrum depends on the energy levels of the activator ions (Er). Emission is observed in the green ( $\sim 0.54\text{ }\mu\text{m}$ ), red ( $\sim 0.66\text{ }\mu\text{m}$ ), and blue ( $\sim 0.41\text{ }\mu\text{m}$ ). Since the dominant emitted light from the present sample appears in the green, detailed emission study of this sample has been limited to the green region. (Other gagarinite samples have been investigated which are relatively more efficient in the red. They also appear to be green, due to the greater sensitivity of the eye to green.) The green emission consists of two sets of peaks, one set from  $0.52$  to  $0.53\text{ }\mu\text{m}$ , and the other (containing about 90 percent of the total green emission at room temperature) between  $0.54$  and  $0.55\text{ }\mu\text{m}$ . The variation of emission with excitation intensity indicates that both spectral regions arise from two-step processes. Thus, the shorter and longer wavelength emission regions are due to de-excitation of  $^2\text{H}_{11/2}$  and  $^4\text{S}_{3/2}$  levels, respectively. This conclusion is consistent with thermal behavior. The overall green emission increases with decreasing temperature to a maximum at about  $170^\circ\text{K}$ , with a slow decrease in emission below this value. However, the emission between  $0.52$  and  $0.53\text{ }\mu\text{m}$  decreases monotonically with decreasing temperature, and is smaller by an order of magnitude at  $100^\circ\text{K}$ , a result consistent with thermal depopulation of the higher-energy  $^2\text{H}_{11/2}$  level at reduced temperatures.

Since phosphor upconversion is a nonlinear process, the efficiency varies with pump intensity. For upconversion to green, a two-step process is involved and the efficiency should be linearly proportional to the intensity until saturation is approached; a source of high intensity at a wavelength near  $0.98\text{ }\mu\text{m}$  is required to approach saturation. Further, since the process is slow, with a rise time of the order of  $10\text{ msec}$ , any pulse technique requires pulse lengths of the

<sup>†</sup> We are indebted to Dr. F. W. Ostemayer of the Bell Telephone Laboratories, Murray Hill, New Jersey, for supplying us with this sample.

same order of magnitude, which effectively eliminates Q-switched lasers as a potential light source. Using a pulsed xenon source, we obtained pulses of 130 Å for 12 msec. The resulting output in this case, after passing through Corning filters 7-56 and 7-69 and a lens system, forms a 1.7-mm spot of almost  $2.5 \text{ W/cm}^2$  at the sample. For this input, green upconversion efficiency of 0.2 percent is achieved for the system. Losses due to the wideband input spectra and the high reflectivity of the sample are included in this system-efficiency figure.

Reducing the input, we found that the efficiency is proportional to the input, for input intensities less than or equal to  $1.2 \text{ W/cm}^2$ . At  $2.5 \text{ W/cm}^2$ , there is a drop from the predicted value. However, significant local heating is evidenced at this high input level and must be eliminated before it can be established whether or not saturation is being approached. At the highest input level attained, the red and blue upconversion efficiencies of the system were 0.018 and  $5 \times 10^{-4}$  percent, respectively, with no indication of saturation.

We are attempting to increase the effective input with a pulsed xenon lamp by improving the optical system between source and sample as well as the heat-sinking of the sample. In addition, other sources such as GaAs:Si diodes and Nd-YAG lasers will be investigated.

N. Menyuk  
K. Dwight  
J. W. Pierce

## 2. Infrared Stimulation of Visible Luminescence in ZnS Phosphors

Measurements similar to those previously carried out on a ZnS:Cu,Al sample<sup>2</sup> have been repeated using a ZnS sample that is nominally undoped but contains enough impurities to be luminescent, and is also infrared stimuable. The luminescence occurs in a green and in a blue band. The intensities of these bands depend on ultraviolet (UV) pump energy such that for higher energies the blue band is very intense and completely dominates the luminescence, while for lower energies both bands are weak with the green band somewhat stronger than the blue band. The response to stimulation by infrared radiation of about  $9 \mu\text{m}$  is qualitatively identical to that observed for ZnS:Cu,Al. When the infrared is abruptly turned on (with steady-state UV pumping), a transient burst of additional luminescence decays back to the no-infrared level. The rise time of the transient pulse is much shorter than the decay time. If the infrared is turned off at any time before the slow decay is complete, the luminescence abruptly returns to the no-infrared level with a fall time comparable to the rise time. The spectrum of stimulated light (at the peak of the transient pulse) is nearly identical to the spectrum of the steady-state UV-induced luminescence (for a particular UV pump energy) except that the green and blue peaks are shifted slightly to higher energy.

A computer solution of the rate equations describing the stimulation model formulated previously<sup>2</sup> has been obtained, but only very recently, and thus far there are results for only one set of values of the various parameters in the equations. Qualitatively, the solutions are in accord with experimental results, in that they predict a blue-shifted transient burst of light with a rise time short compared with the fall time in response to an abrupt application of infrared under conditions of steady-state UV pumping. However, a detailed comparison with experiment has not yet been made.

We are now setting up to take thermal glow curve measurements and photoconductivity measurements, the latter to try to detect the effect of infrared stimulation on the conduction-band population.

J. W. Allen

## B. LASER SPECTROSCOPY

### 1. Resolved Q-Branch Absorption in Nitric Oxide: Nuclear Hyperfine Splitting

Our previous high-resolution spectroscopic studies of the fundamental vibration-rotation band of nitric oxide have been restricted to the R-branch.<sup>3</sup> Using a  $\text{PbS}_{0.6}\text{Se}_{0.4}$  semiconductor diode laser operating near  $5.4\text{ }\mu\text{m}$ , we have fully resolved for the first time several lines near the head of both the  $Q_{1/2}$  and  $Q_{3/2}$  branches. Both  $\Lambda$ -type doubling and nuclear hyperfine structure (hfs) are observed for the first few  $Q_{1/2}$  absorption lines. This is the first detection of hfs in the infrared vibration-rotation spectrum of a molecule. Previous observations of hfs in molecular spectra have been restricted largely to the radiofrequency<sup>4</sup> and microwave<sup>5</sup> regimes. Measurements of hfs in the visible<sup>†</sup> and infrared regimes have been greatly hampered by the enormous resolution ( $>10^6$ ) required as a result of the smallness of typical molecular hyperfine energies ( $\lesssim 100\text{ MHz}$ ).

The semiconductor laser was mounted on the cold finger of a liquid helium dewar at a temperature of  $\sim 10^\circ\text{K}$  and was placed in the field (perpendicular to the junction) of an 18-kG electromagnet. The laser frequency was tuned by varying the diode current with a measured tuning rate of  $30\text{ MHz/mA}$ . Gross magnetic-field tuning of the laser (as much as  $4\text{ cm}^{-1}$  for 18 kG) was essential, and served to match the laser output with the NO molecular lines at the head of the Q-branch ( $1876\text{ cm}^{-1}$ ). The laser tuning rate was determined by matching the observed absorption linewidths with the calculated Doppler widths and is estimated to be accurate to  $\pm 5$  percent. A typical current-tuning rate for the laser used in these experiments was  $30\text{ MHz/mA}$ .

Nitric oxide is the only stable diatomic molecule which has electronic angular momentum in its ground state ( $^2\Pi$ ) and, therefore, electric-dipole-allowed Q-branch vibration-rotation bands ( $\Delta v = 1, 2, 3, \dots, \Delta J = 0$ ). The individual lines near the head of the Q-branch are very closely spaced, since there is no change in rotational energy involved, and they have not been resolved using conventional spectroscopic techniques.<sup>7,8</sup> A fully resolved absorption spectrum of several absorption lines near the head of the fundamental ( $\Delta v = 1$ ) Q-branch of NO is shown in Fig. IV-1. The data are the transmission through a 10-cm cell of NO at 10 torr as a function of diode current. An approximate frequency scale is shown. Beginning at high current (high frequency), the first lines result from transitions in the  $^2\Pi_{1/2}$  electronic ground state. The gross splitting into symmetric pairs as marked results from  $\Lambda$ -doubling which we observed previously<sup>3</sup> for R-branch lines. In contrast to R- and P-branch lines, the  $\Lambda$ -doubling frequency increases rapidly with increasing  $J$  (approximately linearly). This results because the  $\Lambda$ -type splitting of Q-branch lines is the sum of the splittings of the initial and final energy level splittings, while for R- and P-branch lines it is the difference of the two. The fine structure appearing on each of the  $\Lambda$ -doublet lines for  $J = 1/2, 3/2$ , and  $5/2$  results from coupling of the electrons to the spin ( $I = 1$ ) of the  $^{14}\text{N}$  nucleus of  $^{14}\text{N}^{16}\text{O}$ . For R- and P-branch transitions, this nuclear

<sup>†</sup> Hfs in electronic transitions of  $\text{I}_2$  and  $\text{Br}_2$  has been observed in the visible; see Ref.6.



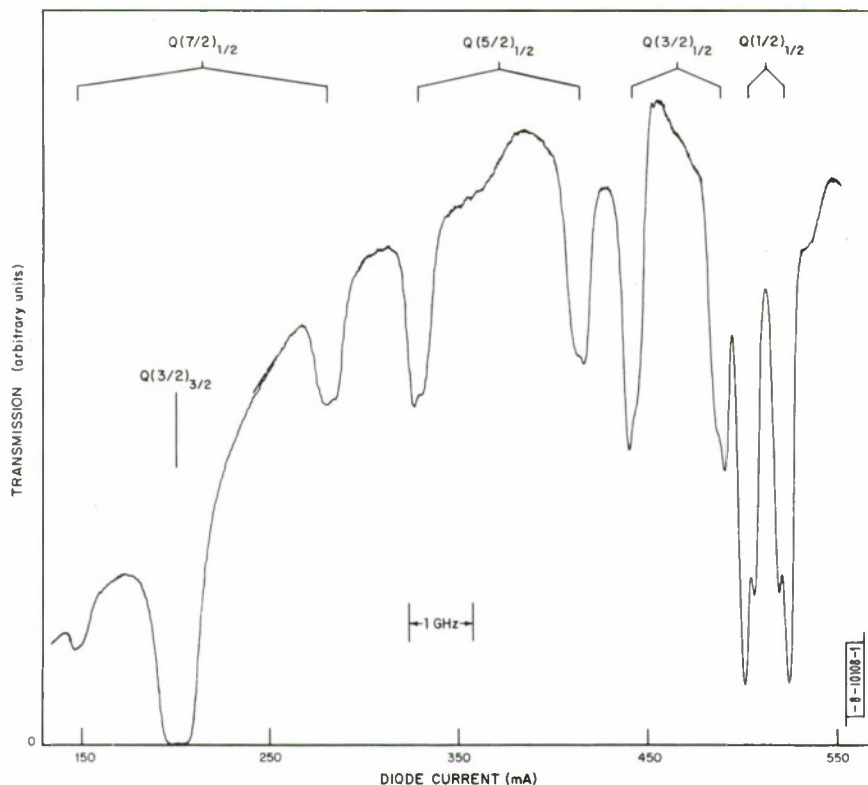


Fig. IV-1. Absorption spectrum of 10-cm cell of NO at 10 torr near head of fundamental Q-branch.

hyperfine splitting is much smaller (particularly for large  $J$  values) and is completely obscured by the room-temperature Doppler width. The hyperfine splitting of the  $Q(1/2)_{1/2}$  line near<sup>7,8</sup>  $1876.1 \text{ cm}^{-1}$  is shown more clearly in the absorption spectrum of Fig. IV-2(a) which was taken with an NO pressure of 1 torr. Note that the  $Q(3/2)_{3/2}$  line of Fig. IV-1 is much stronger than the  $Q_{1/2}$  lines. Also, the  $\Lambda$ -doubling of the  $Q_{3/2}$  branch is very small. For the  $Q(3/2)_{3/2}$  line, it is expected to be only about 6 MHz, which is much less than the Doppler width.

From microwave measurements<sup>9</sup> on the vibrational ground state ( $v = 0$ ), it is known that the electron-nuclear coupling in NO is predominantly magnetic dipole<sup>10,11</sup> in origin, the electric quadrupole contribution being much smaller. In fact, for  $J = 1/2$ , the electric quadrupole terms vanish identically.<sup>11</sup> The electronic magnetic moment couples the molecular momentum  $\vec{J}$  to the  $^{14}\text{N}$  spin  $\vec{I}$ , yielding the resultant momentum  $\vec{F}$ . The appropriate quantum numbers are  $\Lambda$ ,  $J$ , and  $F$  with the energies given by<sup>9-11</sup>

$$E_{\pm} = \pm \frac{1}{2} E_{\Lambda}(J) + P_{\pm}(J) (\vec{I} \cdot \vec{J}) \quad (\text{IV-1})$$

where  $E_{\Lambda}(J)$  is the  $\Lambda$ -doubling energy,  $P_{\pm}(J)$  is the magnetic hyperfine coupling constant, and  $\vec{I} \cdot \vec{J} = (1/2) [F(F+1) - J(J+1) - I(I+1)]$ . For  $J = 1/2$ , the allowed values of  $F$  are  $1/2$  and  $3/2$ , and each of the  $\Lambda$ -doublet energy levels split into two levels as shown schematically in Fig. IV-2(a-b). The selection rules for Q-branch electric dipole transitions are  $\Delta J = 0$ ,  $\Delta F = 0, \pm 1$ , and opposite symmetry in the initial and final  $\Lambda$ -doublet states,  $\Lambda_{+} \rightarrow \Lambda_{-}$  or  $\Lambda_{-} \rightarrow \Lambda_{+}$ . The four allowed

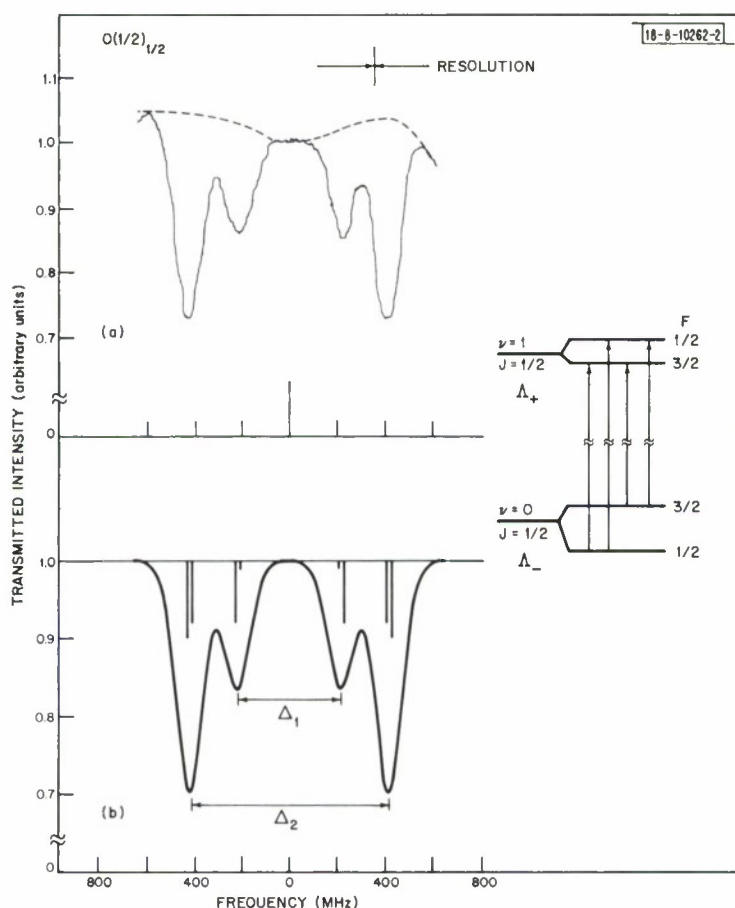


Fig. IV-2. For  $Q(1/2)_{1/2}$  transition, (a) transmission through 10-cm cell of NO at 1 torr vs frequency, and (b) theoretical absorption spectrum (see text). Energy level diagram of right shows schematically nuclear hyperfine splitting and associated transitions.

hyperfine transitions are shown schematically in Fig. IV-2 for one of the two allowed  $\Lambda$ -doublet transitions. Neglecting the vibrational dependence of the fine structure constants of Eq. (IV-1), we calculated the theoretical absorption spectrum of Fig. IV-2(b) using  $E_{\Lambda}(1/2) = 708$  MHz,  $P_+(1/2) = -13.14$  MHz, and  $P_-(1/2) = 136.9$  MHz taken from microwave measurements<sup>9</sup> on the vibrational ground state ( $v = 0$ ). There are a total of eight hyperfine lines whose relative strengths<sup>12</sup> and positions are given by the vertical lines. We have assumed a Gaussian-Doppler profile<sup>13</sup> for each line with a calculated full width of 127 MHz. The calculated absorption strength was adjusted arbitrarily to approximate that of the experimental data. The hyperfine lines fall into four nearly degenerate pairs with a separation small compared with the Doppler width, resulting in four apparent absorption peaks. It is clear that the overall agreement between the theoretical spectrum of Fig. IV-2(b) and the data of Fig. IV-2(a) is excellent. For example, the calculated ratio of the absorption strengths of the hyperfine split pairs is 1.82, while the measured ratio is 1.86.

F. A. Blum    A. R. Calawa  
K. W. Nill    T. C. Harman



## Section IV

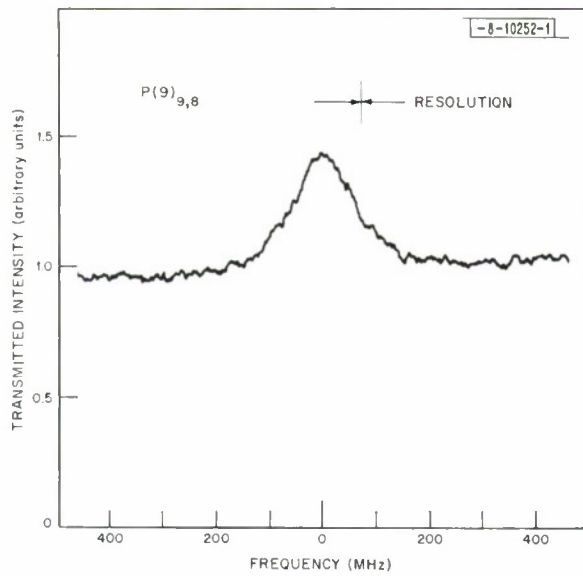
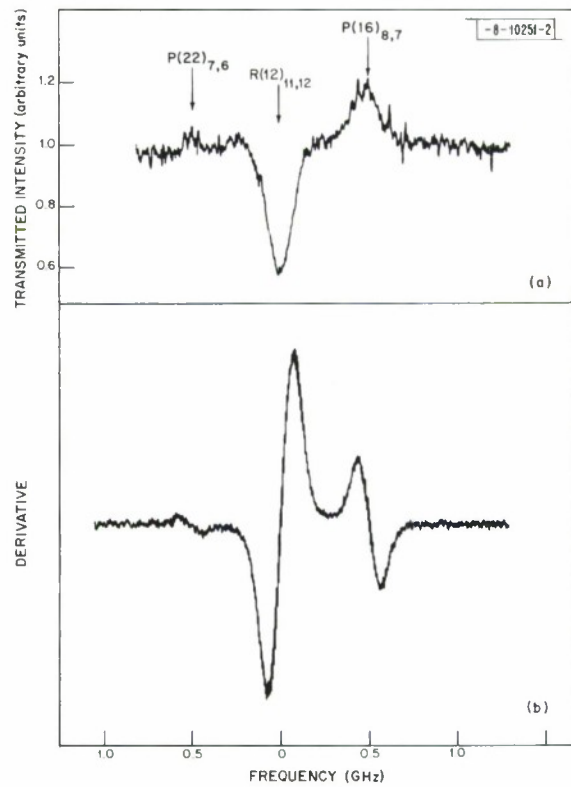


Fig. IV-3. Gain lineshape of  $P(9)_{9,8}$  line of CO laser amplifier.

Fig. IV-4. Spectra of three CO laser amplifier lines near  $1897.6 \text{ cm}^{-1}$ : (a) transmission spectrum for discharge current of 26 mA; (b) derivative spectrum for discharge current of 15 mA.



## 2. Measurement of the Gain Lineshape of a CO Gas Laser Using a Tunable Semiconductor Laser

We have measured the full gain (loss) lineshape of several vibration-rotation lines of a carbon monoxide gas laser amplifier using a tunable PbSSe semiconductor laser operating near  $5.3\text{ }\mu\text{m}$ . With a linewidth of  $<1\text{ MHz}$ , the current-tuned semiconductor laser completely resolves the gain (loss) lineshape of each individual line. R-branch lines exhibited loss under all conditions, while P-branch lines showed gain and/or loss depending on the discharge conditions. Previous measurements of the single-pass gain of gas lasers have been restricted generally to discrete frequency measurements using a matched laser and amplifier.<sup>14,15</sup>

The 4-cm-diameter CO laser tube was liquid nitrogen cooled<sup>16</sup> over 72 cm of a 90-cm discharge length. Discharge was formed in a flowing gas mixture of CO, He,  $\text{N}_2$ , and air with nominal partial pressures at the output end of 2, 9, 2, and 1.5 torr, respectively. The laser tube was terminated with Brewster windows and emitted about 0.5-W CW in single-line operation as an oscillator with an optical cavity formed by a diffraction grating and a dielectric-coated germanium mirror. The semiconductor diode laser was fabricated from single-crystal  $\text{PbS}_{0.6}\text{Se}_{0.4}$  as previously described.<sup>17</sup> Its nominal multimode power output was  $70\text{ }\mu\text{W}$  with a DC bias current of about 1 A. The current-tuning rates were determined by measuring the amount of current change necessary to tune between the  $\Lambda$ -doublet peaks of  $\text{R}_{1/2}$  lines of NO in calibration cells,<sup>3</sup> and are estimated to be accurate to  $\pm 5$  percent. The signal transmitted through the laser amplifier was confined to a central region having a diameter of 1 cm using an external aperture.

Figure IV-3 shows the frequency gain profile of the CO laser operating on the  $\text{P}(9)_{9,8}$  line of CO at  $^{18,19} 1900.05\text{ cm}^{-1}$  for a discharge current of 8 mA. Note the full resolution of the lineshape. The line center single-pass gain is 43 percent. Assuming that gain occurs only over the cooled length, the single-pass gain coefficient is  $0.005\text{ cm}^{-1}$ . This gain coefficient is somewhat larger than typical ones reported by Harvey and Barry,<sup>14</sup> and smaller than the peak gain coefficient of  $0.008\text{ cm}^{-1}$  for the  $\text{P}(9)_{9,8}$  line reported by Bhaumik, *et al.*<sup>15</sup> The full width at half gain coefficient for this line is 132 MHz. We estimate the collision width<sup>20</sup> to be 60 MHz, yielding a Doppler width of 100 MHz. Using the 100-MHz Doppler width, we obtain directly translational CO temperature of  $170^\circ\text{K}$  as compared with the tube wall temperature of  $77^\circ\text{K}$ . Our measured temperature is in rough agreement with previous estimates<sup>14-16</sup> (ranging from about  $140^\circ$  to  $200^\circ\text{K}$ ) based on thermal considerations and theoretical fits to gain measurements. The gain profile of this line was studied also as a function of discharge current and gas pressure.

Three closely spaced CO molecular lines observed near  $1897.6\text{ cm}^{-1}$  are shown in Fig. IV-4(a-b). There is a weak gain line, followed by a strong loss line and a stronger gain line as shown in Fig. IV-4(a). The weak gain line is more apparent in Fig. IV-4(b) which shows a derivative spectrum taken by frequency modulating the semiconductor laser with a small AC current component. The two gain lines are P-branch, while the loss line is R-branch. Loss on R-branch lines is expected on the basis of previous measurements and the known partial inversion in the CO laser.<sup>14,16,19,21</sup> Note that the loss on the R-branch line could not be measured in a conventional matched laser-amplifier system. Table IV-1 gives the line identifications and associated peak gains and losses of Fig. IV-4(a). The line positions were calculated<sup>18</sup> using the molecular parameters of Mantz, *et al.*<sup>19</sup> Taking the  $\text{R}(12)$  line as a reference point, we find the  $\text{P}(16)$  line to lie 503 MHz above and the  $\text{P}(22)$  line to lie 520 MHz below. The calculated spacings are 660 MHz above and 380 MHz below, respectively. The measured relative positions are

TABLE IV-1  
OBSERVED CO LINES NEAR  $1897.6 \text{ cm}^{-1}$

$\nu_1 \rightarrow \nu_2$	Branch (J)	Calculated Frequency ( $\text{cm}^{-1}$ )	Separation $\Delta f$ (MHz)		Gain (Loss) (percent)
			Measured	Calculated	
$8 \rightarrow 7$	P(16)	1897.661	503	660	18
$11 \rightarrow 12$	R(12)	1897.639	0*	0	(43)
$7 \rightarrow 6$	P(22)	1897.632	520	380	5
* Taken as zero far reference.					

considerably more accurate than the calculated ones since the calculated line positions are accurate only to  $\pm 180 \text{ MHz}$ .

Three other CO lines which exhibited loss were observed. Two were R-branch, as expected: R(13)<sub>11,12</sub> at  $1900.6 \text{ cm}^{-1}$ , and R(4)<sub>10,11</sub> at  $1898.6 \text{ cm}^{-1}$ . The third line, P(2)<sub>9,10</sub> at  $1900.4 \text{ cm}^{-1}$ , exhibited loss even though it was in the P-branch. This is expected since theoretical calculations<sup>21</sup> for weakly inverted CO bands indicate that P-branch lines with small J typically exhibit loss. The P(2)<sub>9,10</sub> and R(13)<sub>11,12</sub> lines were observed to lie  $0.308$  and  $0.525 \text{ cm}^{-1}$  above P(9)<sub>9,8</sub>. These separations are to be compared with the calculated ones of  $0.327$  and  $0.544 \text{ cm}^{-1}$ . Again, the measured separations are well within the error of the calculated values.

Finally, the utility of gain and loss profile measurements on gas lasers using tunable semiconductor lasers as reported here should be emphasized. The technique is simple and direct, and may prove particularly valuable in the study of complex systems such as the CO and CO<sub>2</sub> lasers.

F. A. Blum    A. R. Calawa  
K. W. Nill    T. C. Harman

### 3. Tunable PbTe Laser Spectroscopy at $6.5 \mu\text{m}$

Using PbTe diode lasers emitting near  $6.5 \mu\text{m}$ , we have obtained high-resolution spectra of methane (CH<sub>4</sub>), nitrogen dioxide (NO<sub>2</sub>), and water vapor. The CW lasers were fabricated from vapor-grown PbTe single crystals. The as-grown p-type crystals were isothermally annealed, and an n-type surface layer  $\approx 40 \mu\text{m}$  thick was produced by diffusion from a metal-rich PbTe source. Laser cavities formed by cleavage were typically about  $0.25 \times 0.65 \text{ mm}$ . The lasers were mounted on the cold finger of a liquid helium dewar at a temperature of  $\lesssim 10^\circ \text{K}$ .

Data were taken on CH<sub>4</sub> using a 10-cm cell with a gas pressure of 20 torr. The CH<sub>4</sub> absorption lines in this region are weak and heavily overlap atmospheric water-vapor bands. However, using derivative spectroscopy, about ten absorption lines in the vicinity of  $1540 \text{ cm}^{-1}$  could be readily attributed to the  $\nu_2$ -band<sup>22</sup> of CH<sub>4</sub>. Figure IV-5 shows<sup>†</sup> the absorption spectrum of a pair of closely spaced lines near  $1541 \text{ cm}^{-1}$ . These lines are apparently the Q(7)<sub>2,1</sub> and Q(7)<sub>1,2</sub>

<sup>†</sup> The weak periodic oscillations on the trace are due to interferometer-type interference between two reflecting surfaces in the optical apparatus.

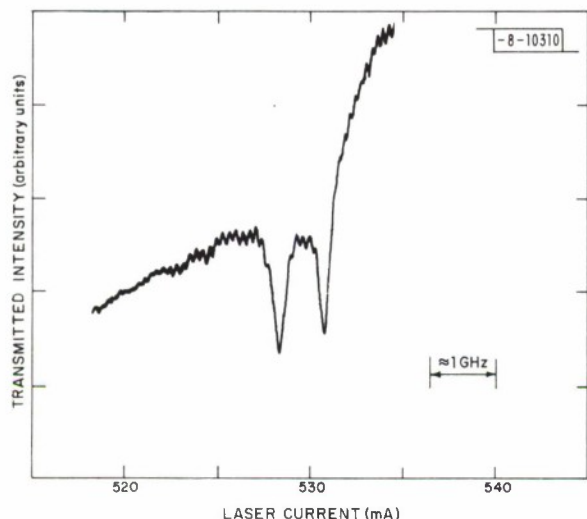


Fig. IV-5. Transmission through 10-cm cell containing 20 torr of  $\text{CH}_4$  as a function of laser current.

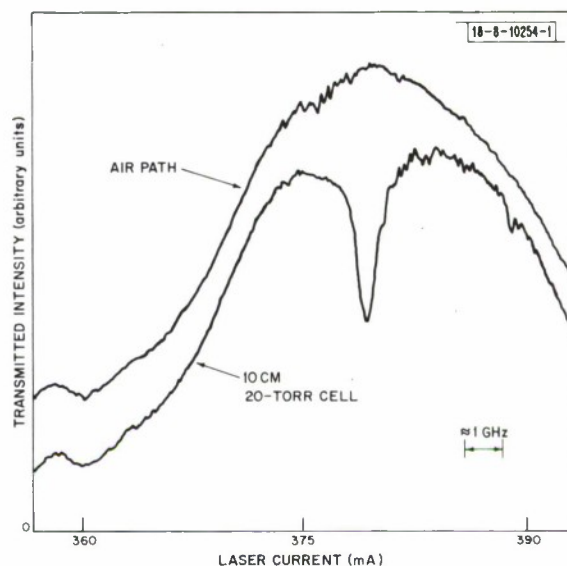


Fig. IV-6. Transmission through 20 torr of water vapor in 10-cm cell as a function of laser current.

lines of the  $\text{CH}_4$   $\nu_2$ -band. The calculated positions of Herranz, *et al.*<sup>23</sup> are  $1541.30$  and  $1541.25\text{ cm}^{-1}$ , respectively; their calculated relative intensities of 349 and 353 are almost equal in agreement with the data of Fig. IV-5. The Doppler width of  $\text{CH}_4$  at this wavelength and room temperature is 134 MHz. Estimating the unknown collision broadening of  $\text{CH}_4$  to be a few megahertz/torr, the widths of the observed lines are probably about 175 MHz. This yields a tuning rate of about 300 MHz/mA for the laser mode used in these experiments. We then estimate the separation of the two absorption lines to be about  $0.024\text{ cm}^{-1}$ , in reasonable agreement with the calculated separation of  $0.05\text{ cm}^{-1}$ .

Some data were taken on  $\text{NO}_2$  which also has numerous absorption lines in the  $\tilde{\nu}_3$ -band in this spectral region.<sup>23</sup> Several weak lines were observed near  $1533\text{ cm}^{-1}$  using derivative techniques and high gas pressures (10 to 50 torr). The weakness of the signals prevented positive identification of the observed lines. The  $\text{NO}_2$  is a heavy molecule having a Doppler width of only 84 MHz at  $1533\text{ cm}^{-1}$ . By measuring the amount of current necessary to tune the laser through the full width of the observed lines, we estimate a tuning rate of about 40 MHz/mA for the device used in these experiments. Note that, even though the two devices used to study  $\text{CH}_4$  and  $\text{NO}_2$  were made from the same crystal, their tuning rates differ by almost an order of magnitude. We have also observed wide variations in tuning rates for PbSSe diode lasers of various compositions.

Finally, absorption spectra of several low-pressure water-vapor lines were taken. The laser used for these measurements was also used in the study of  $\text{CH}_4$  with a nominal fine-tuning rate of 300 MHz/mA. Figure IV-6 shows the absorption spectrum (near  $1534\text{ cm}^{-1}$ ) of a 10-cm cell of 20-torr water vapor. The background trace was taken without the cell in the radiation path and is displaced for clarity. The  $\sim 0.5\text{ m}$  path between the laser and the detector was occupied by ambient air. Note that, while the absorption line shows up well in the low-pressure cell, collision broadening in the ambient air completely obliterates the line. The width of the line is



about 480 MHz ( $0.016 \text{ cm}^{-1}$ ) and its strength is  $>0.038 \text{ cm}^{-2}/\text{atm}$ . The only known water-vapor line of comparable strength in this vicinity<sup>24</sup> is the  $2(1, 2) \leftarrow 3(0, 3)$  transition of the  $\nu_2$ -band at a calculated wavelength of  $1533.82 \text{ cm}^{-1}$ . This line has a calculated strength of  $0.009 \text{ cm}^{-2}/\text{atm}$  and an estimated<sup>25</sup> width of  $0.03 \text{ cm}^{-1}$  due to self-broadening.<sup>24</sup> The large discrepancy in line strengths is not understood.

F. A. Blum    A. R. Calawa  
K. W. Nill    T. C. Harman

#### 4. Molecular Systems Optically Pumped with TEA Lasers

Submillimeter radiation has recently been obtained from molecular gases optically pumped with  $\text{CO}_2$  and  $\text{NO}_2$  lasers on a quasi-CW basis.<sup>26</sup> We have extended this technique to the high-power regime by the use of  $\text{CO}_2$  TEA lasers ( $\sim 0.7 \text{ MW}$ ) which enable the acquisition of higher peak powers in the far-infrared than previously obtainable. In addition to increasing the output power, the extremely high TEA laser pump power permits the observation of several other types of processes.

One process is the pumping of rotational levels in molecular gases even when the absorption overlap with the  $\text{CO}_2$  source is relatively poor. This can be attributed to the following factors: (a) operation is above threshold in the wings of a highly pressure-broadened Lorentzian lineshape (molecular gas pressure  $\sim 1$  torr), (b) the high peak fields of the TEA laser produce a high-frequency Stark perturbation of the rotational excited states, and (c) the  $\text{CO}_2$  TEA laser itself has an extremely wide frequency output since it is operating at atmospheric pressures.

Because of these effects, we have found a large number of new lines in  $\text{CH}_3\text{OH}$  and  $\text{CH}_3\text{F}$  not previously reported. Their wavelengths, measured using a scanning Fabry-Perot and box-car, are listed in Table IV-2. The delays of the emissions after the termination of pump power are also listed, but cannot be explained using our current model. It should be noted that any

TABLE IV-2				
NEW OPTICALLY PUMPED FAR-INFRARED LASER LINES				
Gas	Pump		Delay ( $\mu\text{sec}$ )	Far-Infrared Radiation ( $\mu\text{m}$ )
$\text{CH}_3\text{OH}$	9.488	P12	2.5	163.9
	9.536	P18	2	205.3
$\text{CH}_3\text{F}$	9.166	R42	2	195.0
	9.174	R40	1	200.3
	9.192	R36	1	215.3
	9.639	P30	1.5	190.9
$\text{CH}_3\text{Cl}$	9.29	R16	2	364.5
	9.488	P12	3	273.7
	9.604	P26	2	263.4
	9.639	P30	2	250.4
	10.22	P24	1	397.6



molecular gas having a permanent dipole moment and capable of being used for Q-switching the CO<sub>2</sub> laser should achieve a rotational population inversion under these conditions. The lines obtained from CH<sub>3</sub>Cl for the first time were established on this basis. In addition to the generation of far-infrared emission, the presence of a permanent dipole moment suggests the possibility of Stark-tuning the output over several hundred megacycles. This is currently under investigation.

H. R. Fetterman    H. R. Schlossberg<sup>†</sup>  
C. D. Parker        J. Waldman

## C. INFRARED PROPERTIES OF SOLIDS

### 1. High-Resolution Far-Infrared Investigation of Hydrogenic Impurities in Ultrapure Germanium

The photoconductivity spectral response of recently developed n-type ultrapure ( $\sim 2 \times 10^{10}$  donors cm<sup>-3</sup>) germanium<sup>‡</sup> has been observed with 0.07-cm<sup>-1</sup> resolution using a Fourier spectrometer in the range 60 to 120 cm<sup>-1</sup> at temperatures in the vicinity of 4.2°K. The photoconductivity-vs-wavelength spectrum shown in Fig. IV-7 exhibits extremely sharp (resolution-limited) and previously unobserved structure due to higher excited states of the hydrogen-like shallow donors in germanium. Four distinct hydrogenic-like series of transitions (labeled A, B, C, and D in Fig. IV-7) have been observed. Based on previous low-resolution studies on doped germanium, series A and B have been identified with antimony and phosphorous donors, respectively. The donors giving rise to series C and D have not yet been identified. Measured spectral response dependence on temperature is consistent with the interpretation of photoconductivity as a two-step process whereby ground state 1s(A) electrons are optically excited to a higher level from which a thermal process further excites a fraction to the conduction band.

Transitions from 1s(A) to higher p<sup>±</sup> and f<sup>±</sup> levels (most of which were observed for the first time in these experiments) have been identified. The energies of the higher-lying levels are found to agree very closely with a theoretical calculation<sup>27</sup> for hydrogenic donors in germanium. Table IV-3 lists the energy differences found between assigned transitions and those calculated for series A and B.

Further high-resolution experiments using Fourier spectroscopy and far-infrared laser spectroscopy should form the basis for unambiguous optical determination of impurity species and quantity in ultrapure samples.

S. D. Seccombe  
D. M. Korn

### 2. Far-Infrared-Reflectivity Study of Paratellurite

The room-temperature far-infrared reflectivity of paratellurite, TeO<sub>2</sub>, has been studied. Due to the presence of optical activity, transparency from 0.33 to 6.5 μm, strongly birefringent refractive indices, an extremely slow <110> shear wave, and a lack of center of inversion, paratellurite lends itself for use in interesting piezoelectric, acousto-optic, and nonlinear optical applications. The zone center optical modes of this D<sub>4</sub><sup>4</sup> structure of TeO<sub>2</sub> decompose into the symmetries 4A<sub>1</sub> + 4A<sub>2</sub> + 5B<sub>1</sub> + 4B<sub>2</sub> + 8E. The infrared-active modes are z-polarized A<sub>2</sub> singlets and the x, y-polarized E doublets.

<sup>†</sup> Laser Physics Section, Air Force Cambridge Research Laboratories.

<sup>‡</sup> Kindly supplied by Dr. R. Hall, General Electric Research and Development Center.

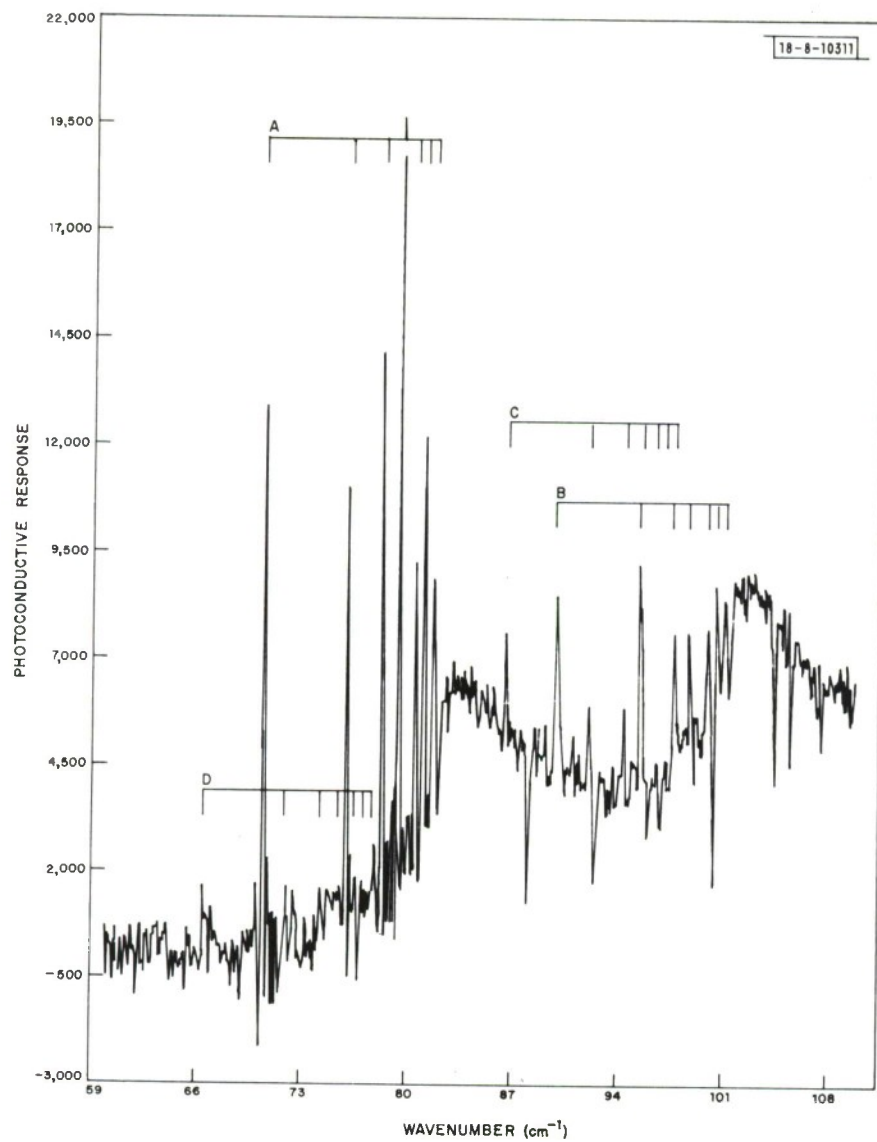


Fig. IV-7. Photoconductivity spectra of ultrapure germanium ( $n \sim 2 \times 10^{12} \text{ cm}^{-3}$ ).

TABLE IV-3 COMPARISON OF TRANSITION ENERGY DIFFERENCES (meV) OBSERVED IN ULTRAPURE GERMANIUM COMPARED WITH THEORY			
Energy Differences	Series A [ $2p^{\pm} - 1s(A) = 8.72$ ]	Series B [ $2p^{\pm} - 1s(A) = 11.15$ ]	Theory
$3p^{\pm} - 2p^{\pm}$	0.69	0.69	0.70
$4p^{\pm} - 2p^{\pm}$	0.97	0.97	1.00
$4f^{\pm} - 2p^{\pm}$	1.12	1.11	1.12
$5p^{\pm} - 2p^{\pm}$	1.26	1.26	1.20
$5f^{\pm} - 2p^{\pm}$	1.32	1.33	1.32
$6f^{\pm} - 2p^{\pm}$	1.40	1.40	1.41

The near-normal incidence room-temperature reflectivity of paratellurite was obtained on a Fourier spectrometer from 50 to  $400\text{ cm}^{-1}$ . Polarized light was obtained with a wire grid polarizer. Spectra were normalized to first surface aluminum mirrors. Figures IV-8 and IV-9 show normalized reflectivities for the two cases studied,  $\vec{E} \parallel c\text{-axis}$  (polarized light) and  $\vec{E} \perp c\text{-axis}$  (unpolarized light). Also displayed in the figures are the reflectivities as calculated

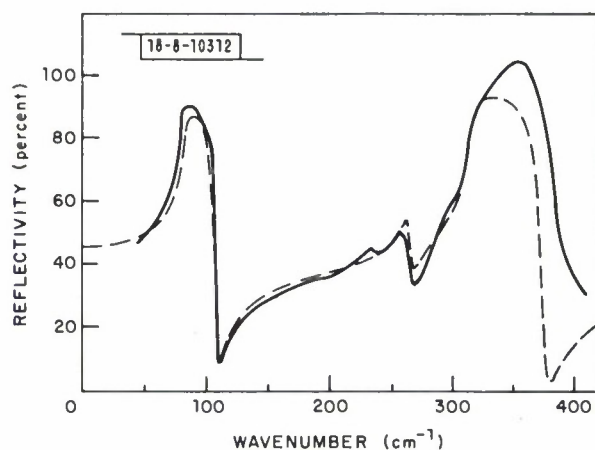


Fig. IV-8. Experimentally obtained reflectivity of paratellurite for  $\vec{E} \parallel c\text{-axis}$  (solid line) and calculated reflectivity (dashed line).

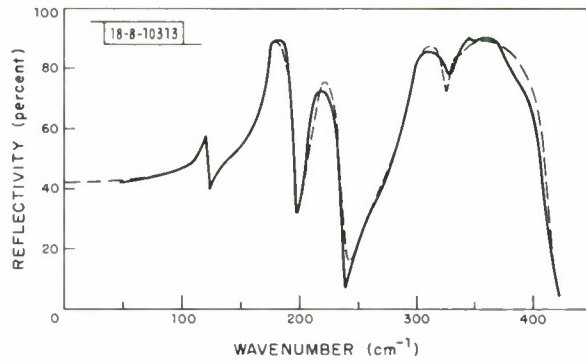


Fig. IV-9. Experimentally obtained reflectivity of parotellurite for  $\vec{E} \perp c$ -axis (solid line) and calculated reflectivity (dashed line).

from previously obtained Raman LO-TO frequency and linewidth data. Work is presently being directed to extend the spectral range of this study and to obtain low-temperature ( $\sim 77^\circ \text{K}$ ) data.

D. M. Korn    T. B. Reed  
A. S. Pine    G. F. Dresselhaus

### 3. Microscopic Theory of the Spontaneous Spin-Flip Raman Lineshape in InSb

The spontaneous spin-flip linewidth is an important parameter which affects the gain, threshold power, and fine-tuning characteristics of the spin-flip Raman laser. In an effort to understand the lineshape, we have considered the effects of ionized impurity scattering at low temperatures in n-type InSb. A Bethe-Salpeter transport equation has been derived which is more general, but analogous in form, to a Boltzmann transport equation, and with the usual "scattering-in" and "scattering-out" terms. In the absence of nonparabolicity and Doppler broadening, the effects of these terms on the Raman lineshape essentially cancel and the effect of the impurities is to replace the Fermi functions with exact distribution functions. Including the effects on nonparabolicity, Doppler broadening, and (in an approximate fashion) level broadening, we have solved the transport equation and have found results similar to those obtained previously using a phenomenological relaxation-time ansatz.<sup>28</sup>

R. W. Davies

## REFERENCES

1. R. A. Hewes and J. F. Sarver, *Phys. Rev.* 182, 427 (1969).
2. Solid State Research Report, Lincoln Laboratory, M.I.T. (1971:4), p. 45, DDC AD-736501.
3. *Ibid.*, p. 50; K.W. Nill, F.A. Blum, A.R. Calawa and T.C. Harman, *Chem. Phys. Letters* (to be published).
4. See, for example, N.F. Ramsey, *Molecular Beams* (Oxford University Press, London, 1955), Chap. VIII.
5. See, for example, W. Gordy and R.L. Cook, *Microwave Molecular Spectra* (Wiley, New York, 1970), Chap. 9.
6. G.R. Hanes and C.E. Dahlstrom, *Appl. Phys. Letters* 14, 362 (1969); R.S. Eng and J.T. LaTourette, *Bull. Am. Phys. Soc.* 16, 43 (1971); J.D. Knox and Y. Pao, *Appl. Phys. Letters* 18, 360 (1971); T.W. Hansch, M.D. Levenson and A.L. Schawlow, *Phys. Rev. Letters* 26, 946 (1971).
7. J.H. Shaw, *J. Chem. Phys.* 24, 399 (1956).
8. D.B. Keck and C.D. Hause, *J. Mol. Spectry.* 26, 163 (1968); *J. Chem. Phys.* 49, 3458 (1968).
9. J.J. Gallagher, F.D. Bedard and C.M. Johnson, *Phys. Rev.* 93, 729 (1954); P.G. Favero, A.M. Mirri and W. Gordy, *ibid.* 114, 1534 (1959); and references therein.
10. R.A. Frosch and H.M. Foley, *Phys. Rev.* 88, 1337 (1952); G.C. Dousmanis, *ibid.* 97, 967 (1955).
11. M. Mizushima, *Phys. Rev.* 94, 569 (1954); C.C. Lin and M. Mizushima, *ibid.* 100, 1726 (1955).
12. Ref. 5, p. 299.
13. Collision broadening for the experimental pressures is negligible. See L.L. Abels and J.H. Shaw, *J. Mol. Spectry.* 20, 11 (1966).
14. Such single-pass gain measurements for the CO laser have been reported in M.E. Harvey and J.D. Barry, *IEEE J. Quantum Electron.* 7, 370 (1970); also see Ref. 15.
15. M.L. Bhaumik, W.B. Lacina and M.M. Mann, *IEEE J. Quantum Electron.* 8, 150 (1972).
16. R.M. Osgood, W.C. Eppers and E.R. Nichols, *IEEE J. Quantum Electron.* 6, 145 (1970).
17. K.W. Nill, F.A. Blum, A.R. Calawa and T.C. Harman, *Appl. Phys. Letters* 19, 79 (1971), DDC AD-734114.
18. A.H. Ross, private communication.
19. A.W. Mantz, E.R. Nichols, B.D. Alpert and K.N. Rao, *J. Mol. Spectry.* 35, 325 (1970).
20. D.A. Draeger and D. Williams, *J. Opt. Soc. Am.* 58, 1399 (1968).
21. C.K.N. Patel, *Phys. Rev.* 141, 71 (1966).
22. J. Herranz, J. Morcillo and A. Gomez, *J. Mol. Spectry.* 19, 266 (1966).
23. E.T. Arakawa and A.H. Nielsen, *J. Mol. Spectry.* 2, 413 (1958).
24. W.S. Benedict and R.F. Calfee, *Line Parameters for the 1.9 and 6.3 Micron Water Vapor Bands* (U.S. Government Printing Office, Washington, D.C., 1967).
25. W.S. Benedict and L.D. Kaplan, *J. Quant. Spectry. Rad. Transfer* 4, 453 (1964).
26. T.Y. Chang and J.D. McGee, *Appl. Phys. Letters* 19, 103 (1971).
27. R.A. Faulkner, *Phys. Rev.* 184, 713 (1969).
28. F.A. Blum and S.R.J. Brueck, *Bull. Am. Phys. Soc.* 16, 442 (1971).



## V. MICROELECTRONICS

### A. MASK-MAKING LABORATORY

Recent efforts in the mask-making laboratory have been concentrated in (1) reducing defect density, and (2) developing image test targets.

In our last report,<sup>†</sup> we discussed a cleaning and inspection procedure for the 10X master reticle. This procedure has virtually eliminated photorepeated defects.

Even with a perfect reticle, defects (primarily pinholes) were still a problem. One source of these additional pinholes was traced to poor chrome adhesion caused by dirt on, and pits in, the glass surface. This source of pinholes has been eliminated by more complete glass cleaning and inspecting procedures. Prior to chrome deposition, the glass is inspected under a microscope with darkfield illumination, which reveals all pits, scratches, and dust. Unacceptable glass is rejected at this stage. After the acceptable plates are coated with chrome, they are ultrasonically cleaned and inspected with transmitted light for pinholes. Again, any defective plates are rejected. This procedure eliminates pinholes due to defective chrome.

Pinholes in the photoresist on chrome plates are still a problem because such pinholes will cause defects in the chrome during etching of the desired pattern. Although this problem has not been eliminated, it can be controlled by touching up the pinholes with photoresist prior to etching the chrome and by using special developing and etching techniques.

It should be noted that part of our pinhole problem is a result of the negative (darkfield) nature of most of our work. The standard integrated circuit manufacturing process uses mostly positive masks which are much less susceptible to pinholes. Very few of our masks are for such a standard process.

In anticipation of efforts to improve the resolution of our masks, we are developing test charts designed to enable us to optimize our focus settings and exposure times. These charts are also designed to test for uniformity of illumination and resolution, flare, corner rounding, adjacency effects, and spurious images.

These efforts to reduce the defect density and to increase the output of the mask-making laboratory have been seriously hampered by the delays in initiating the pending space changes. Some of these handicaps are:

- (1) Lack of space for our new contact printer.
- (2) No space for clean benches for our inspection microscopes.
- (3) No fume hood for toxic etchants and cleaning solutions.
- (4) Insufficient space for simultaneous processing of emulsion and metal-clad plates.

D. L. Smythe, Jr.

---

<sup>†</sup>Solid State Research Report, Lincoln Laboratory, M.I.T. (1971:4), p.61, DDC AD-736501.

## B. SEMICONDUCTOR DEVICES AREA

Optical Sensor Assembly:- A photodiode array consisting of three diodes on a 50- × 50-mil chip was fabricated for use in the Educational Technology Program. The optically active areas of the photodiodes were required to have sharp cutoffs at the geometric borders. Commercially obtained diodes had acceptable sensitivity but failed to maintain the required sharp cutoff. The primary cause of this seemed to be the use of high-resistivity silicon material and the associated high lifetime which allows carriers produced some distance from the active region to reach and be collected at the photodiode junction. As a first design step, Group 87 employed lower-resistivity material to reduce the lifetime and diffusion length. Although the output signal level was thus down 8 dB at a distance of 1 mil from the active diode border, we decided to attempt further improvements. A sharper cutoff was provided by employing a gold diffusion step to further reduce the lifetime, thus lowering the photoresponse 40 dB at a distance of 0.1 mil from the active diode border. To prevent light bounce and ghosts, the bonding leads which are highly reflective were located as far as possible from the active area of the photodiode by the use of long aluminum conductors from the active area to the bonding pads. The problem of light bounce from the gold-plated header on which the device was mounted was solved by coating the header adjacent to the chip with DAG, a dispersion of colloidal graphite. A dozen diodes were packaged by Group 87 and incorporated by Group 25 in their equipment.

Electron-Beam-Irradiated Diodes (E-Bird):- The specifications for  $V_B \geq 200$ ,  $V_{PT} \leq 50$  V,  $I_S \leq 100 \mu\text{A}$  have been met on n-diffused p-type and p-diffused n-type diodes utilizing channel stoppers in the device design. Several units have been assembled in the new high-power shielded package. A recent electron-beam test of one of the delivered diodes indicates good gain and electrical characteristics. High-temperature storage life tests (100 hours at 200°C) have been carried out on these lots of dice without failure.

Nuclear Particle Detectors:- Beta bombardment tests have been performed using a 30- to 40-mCi 2-MeV beta source ( $\text{Sr}^{90}$ ). The signal-to-noise ratio (which includes noise of the device and the amplifier) is 4 to 1, with no crosstalk discernible between adjacent diodes. The rise time was 40 nsec and the fall time 100  $\mu\text{sec}$ . Detector noise was 20 mV, which is considered to be very satisfactory. A collimator has been made for the beta source which should result in more accurate measurements.

Microwave Transistor:- Work on a process for making high-frequency microwave transistors has been initiated. The process involves extremely shallow diffusions of the order of  $\frac{1}{2} \mu$  base and  $\frac{1}{4} \mu$  emitters. Chrome-gold metalization is used for contacts to avoid alloying through the shallow diffusions such as occurs when conventional aluminum contacts are used. Initial characteristics are  $B_{VCBO} \approx 60$  V,  $B_{VCEO} \approx 60$  V,  $B_{VEBO} \approx 7$  V,  $\beta \approx 50$ . These devices are presently being packaged in a TO-72 package for microwave measurements.

Infrared Detector:- A large 320-mil-diameter optical electronic IR sensor device has been prepared which is to operate at liquid He temperatures. The device consists of 26 shallow boron-diffused contacts with Al bonding pads on one surface and a shallow boron diffusion on the bottom surface of a 4.0-mil-thick Al- or Ga-doped low-resistivity single-crystal silicon wafer. Several of these units have been produced from both the Al- and Ga-doped wafers. Experiments were conducted in mounting the 320-mil-diameter wafer into an alumina-Kovar package using

pure indium solder at 600° C. Mounting in an H<sub>2</sub> atmosphere gave a strong alloyed bond, but the wafer broke under liquid He temperature. Reducing the mounting temperature to approximately 300° C enabled the Si wafer to survive at the liquid He conditions. Experiments are continuing to determine the optimum bonding conditions.

R. A. Cohen

### C. APPLICATIONS OF ELECTRON-BEAM EVAPORATION TECHNOLOGY

Several current programs utilize the unique capabilities of Group 87's electron-beam (EB) evaporation system. This system is diffusion pumped and will routinely reach pressures in the mid-10<sup>-7</sup>-torr range. The vacuum can be extended to the upper 10<sup>-8</sup>-torr range by bakeout of the stainless-steel bell jar prior to evaporation. The use of a high-speed (2400 liters/sec) diffusion pump allows the maintenance of high vacuum during evaporation at high rates. The electron beam will deliver 10 kW into any one of four crucibles in a rotatable, copper hearth. Substrates can be mounted either 6 or 18 inches from the evaporant source. Both positions are equipped with a quartz-crystal thickness monitor, and the 18-inch distant position is protected by a shutter and can be heated to 300° C by quartz iodide heating lamps.

The three programs currently utilizing the major portion of the EB evaporator's available time are for the Microsound Group, the Electronic Materials Group, and the Digital Computers Group. Work for the Microsound Group, although occasionally involving many different films and film combinations, primarily requires the EB evaporation of chromium-gold duplex films under very stringent conditions. The preparation of high-resolution (1-μm lines and spaces), thin-film, surface-wave transducers on piezoelectric crystals such as lithium niobate utilizes a technique<sup>†</sup> which requires that high-quality films of chromium and gold be deposited sequentially from a point source located a considerable distance from the substrate. The EB evaporator is ideally suited for this type of evaporation. The focused electron beam (approximately  $\frac{1}{8}$  inch in diameter) results in an evaporant source which closely approximates a point source, and the 18-inch source-to-substrate distance is sufficient to give effective line-of-sight evaporation. The high initial vacuum, the rapid pumping speed, and the ability to change rapidly from the crucible containing chromium to that containing gold results in the highly adherent, very pure films needed in this work.

The program for the Electronic Materials Group, which is in its initial stages, involves the preparation of transition metal oxide films. Thus far, films of V<sub>2</sub>O<sub>3</sub> have been prepared on glass substrates from a source of V<sub>2</sub>O<sub>3</sub> crystallites contained in an unlined crucible in the copper hearth. X-ray analyses of the resulting films have shown them to be pure V<sub>2</sub>O<sub>3</sub>. Future work will involve the preparation of NiO films by the reactive evaporation of Ni in a partial pressure of O<sub>2</sub>, and the evaporation of V<sub>2</sub>O<sub>3</sub> films onto single-crystal substrates.

The program under way for the Digital Computers Group requires that very high-quality films of several aluminum-silicon alloys be deposited onto silicon wafers to a thickness of approximately 1 μm (10,000 Å). Because these films will be photolithographically processed to form ohmic contacts and interconnections for high-density, active devices in the silicon wafer, the films must be of high purity and must be evaporated very quickly to give the small grain

<sup>†</sup> H. I. Smith, F. J. Bachner and N. Efremow, J. Electrochem. Soc. 118, 821 (1971), DDC AD-729609.



## Section V

size necessary for high-resolution aluminum photolithography. As an added restraint, the source must be evaporated almost to completion because of the different evaporation rates of silicon and aluminum. Films of 50% Si - 50% Al have been successfully prepared by evaporation of a predetermined amount of alloy from an intermetallic liner (Union Carbide HDH grade) placed in a crucible in the copper hearth. To achieve a film thickness of  $1\text{ }\mu\text{m}$  with the limited amount of material that could be placed in a crucible liner, the substrates were held on a rotatable holder, 6 inches above the source. After a small amount of material had been evaporated against a bare portion of the substrate holder, the holder was rotated to bring the silicon substrates into position and the film was deposited.

F. J. Bachner

### D. BONDING AND ASSEMBLY

Nuclear Particle Detector:- The nuclear particle detector, which has been recently tested with good results, presented some unusual bonding problems. The 2-mil thickness of the device required extreme care in handling and bonding. The requirement for metalization on both sides of the array made it necessary to design the structure with 20 beam leads on one side and 20 contact pads on the other. The die was precisely aligned and attached to the substrate with a conductive adhesive.

The metal beams extending from the monolithic array were thermocompression gold-bonded to the package substrate using an eyelet technique. This technique utilizes a hollow tool which allows the metal to flow upward during bonding rather than outward as occurs during wedge bonding, thus permitting us to bond on 2-mil centers and maintain specified separation between beams.

The upper 20 contact pads were thermocompression bonded with the ball and stitch method using 0.7-mil gold wire to maintain adequate separation. The bonds from the substrate to the package output leads had thermocompression ball bonds to complete the assembly to the 40-lead flat package.

EBS Devices:- The low thermal impedance requirement for this device requires special bonding techniques.

The chip is  $75 \times 75$  mils and approximately 5 mils thick. These chips are eutectically bonded to the top of the 120-mil-diameter gold-plated copper posts. A washer-shaped gold shield approximately 1 mil thick is bonded using a wobble bonding technique to the metalized diffused area contact of the diode. The outer edge of this shield is bonded to a ring-shaped metalized ceramic.

Thermal impedance measurements of these devices have been generally well within the  $1^\circ\text{C/W}$  goal. However, about one out of four of the dies develops a crack after bonding; the factors which could cause this are being examined. For example, the importance of the surface finish on the top of the post in minimizing voids between the post and the chip is being weighed. Also being explored is the effect of the thickness of the chip on this breakage. A careful survey of the bonding temperatures and heating times is being made to determine optimum design parameters for this device.

T. F. Clough

DOCUMENT CONTROL DATA - R&D																	
(Security classification of title, body of abstract and indexing annotation must be entered when the overall report is classified)																	
1. ORIGINATING ACTIVITY (Corporate author)  Lincoln Laboratory, M.I.T.		2a. REPORT SECURITY CLASSIFICATION Unclassified  2b. GROUP None															
3. REPORT TITLE  Solid State Research																	
4. DESCRIPTIVE NOTES (Type of report and inclusive dates) Quarterly Technical Summary - 1 November 1971 through 31 January 1972																	
5. AUTHOR(S) (Last name, first name, initial)  McWhorter, Alan L.																	
6. REPORT DATE 15 February 1972	7a. TOTAL NO. OF PAGES 72	7b. NO. OF REFS 71															
8a. CONTRACT OR GRANT NO. F19628-70-C-0230  b. PROJECT NO. 649L  c.  d.		9a. ORIGINATOR'S REPORT NUMBER(S) Solid State Research (1972:1)  9b. OTHER REPORT NO(S) (Any other numbers that may be assigned this report) ESD-TR-72-53															
10. AVAILABILITY/LIMITATION NOTICES  Approved for public release; distribution unlimited.																	
11. SUPPLEMENTARY NOTES  None	12. SPONSORING MILITARY ACTIVITY  Air Force Systems Command, USAF																
13. ABSTRACT  <p>This report covers in detail the solid state research work of the Solid State Division at Lincoln Laboratory for the period 1 November 1971 through 31 January 1972. The topics covered are Solid State Device Research, Quantum Electronics, Materials Research, Physics of Solids, and Microelectronics. The Microsound work is sponsored by ABMDA and is reported under that program.</p>																	
14. KEY WORDS <table><tbody><tr><td>solid state devices</td><td>proton bombardment</td><td>infrared</td></tr><tr><td>quantum electronics</td><td>photodiodes</td><td>Raman scattering</td></tr><tr><td>materials research</td><td>laser spectroscopy</td><td>semiconductor devices</td></tr><tr><td>physics of solids</td><td>crystal growth</td><td>magneto-optical research</td></tr><tr><td>microelectronics</td><td>TEA lasers</td><td></td></tr></tbody></table>			solid state devices	proton bombardment	infrared	quantum electronics	photodiodes	Raman scattering	materials research	laser spectroscopy	semiconductor devices	physics of solids	crystal growth	magneto-optical research	microelectronics	TEA lasers	
solid state devices	proton bombardment	infrared															
quantum electronics	photodiodes	Raman scattering															
materials research	laser spectroscopy	semiconductor devices															
physics of solids	crystal growth	magneto-optical research															
microelectronics	TEA lasers																